

## Structural basis for the inhibition of cGAS by nucleosomes

**Authors:** Tomoya Kujirai<sup>1</sup>†, Christian Zierhut<sup>2,5</sup>†, Yoshimasa Takizawa<sup>1</sup>, Ryan Kim<sup>2</sup>, Lumi Negishi<sup>1</sup>, Nobuki Uruma<sup>1,3</sup>, Seiya Hirai<sup>1,4</sup>, Hironori Funabiki<sup>2\*</sup>, Hitoshi Kurumizaka<sup>1,3,4\*</sup>

### Affiliations:

5 <sup>1</sup> Laboratory of Chromatin Structure and Function, Institute for Quantitative Biosciences, The University of Tokyo, 1-1-1 Yayoi, Bunkyo-ku, Tokyo 113-0032, Japan.

<sup>2</sup> Laboratory of Chromosome and Cell Biology, The Rockefeller University, New York, NY 10065, USA

10 <sup>3</sup> Graduate School of Advanced Science and Engineering, Waseda University, 2-2 Wakamatsucho, Shinjuku-ku, Tokyo 162-8480, Japan.

<sup>4</sup> Department of Biological Sciences, Graduate School of Science, The University of Tokyo, 1-1-1 Yayoi, Bunkyo-ku, Tokyo 113-0032, Japan.

<sup>5</sup> Present address: Division of Cancer Biology, The Institute of Cancer Research, London, SW3 6JB, UK

15

\*Correspondence to: Hironori Funabiki (e-mail: funabih@rockefeller.edu) or Hitoshi Kurumizaka (e-mail: kurumizaka@iqb.u-tokyo.ac.jp)

†These authors contributed equally to this work.

20

**Abstract:** The cyclic GMP-AMP synthase (cGAS) senses invasion of pathogenic DNA and stimulates inflammatory signaling, autophagy and apoptosis. Organization of host DNA into nucleosomes was proposed to limit cGAS autoinduction, but the underlying mechanism was unknown. Here, we report the structural basis for this inhibition. In the cryo-EM structure of the human cGAS-nucleosome core particle (NCP) complex, two cGAS monomers bridge two NCPs by binding the acidic patch of H2A-H2B and nucleosomal DNA. In this configuration, all three known cGAS DNA-binding sites, required for cGAS activation, are repurposed or become inaccessible, and cGAS dimerization, another pre-requisite for activation, is inhibited. Mutating key residues linking cGAS and the acidic patch alleviates nucleosomal inhibition. This study  
25 establishes a structural framework for why cGAS is silenced on chromatinized self-DNA.  
30

**One Sentence Summary:** The cryo-EM structure of the cGAS-nucleosome complex reveals how chromatin inhibits cGAS activation.

35

### Main Text:

The cyclic GMP-AMP synthase (cGAS)-stimulator of interferon genes (STING) pathway senses pathogenic DNA and activates the innate immune system during infections, cancer and autoimmune diseases (1,2). DNA sensing is achieved by three distinct DNA binding surfaces on

cGAS (sites A-C) (3). DNA allosterically activates cGAS to synthesize cyclic GMP-AMP (cGAMP) (3-6), which then associates with STING (6-11), promoting autophagy, inflammation, senescence, or apoptosis (8,9,12). A central question is how cGAS avoids activation by self-DNA. Although the nuclear envelope may limit cGAS from accessing chromosomes (1,2), cGAS signaling is attenuated even when cGAS is forced into the nucleus (13). Following mitotic nuclear envelope disassembly, cGAS rapidly associates with chromosomes (14,15), but signaling is largely suppressed (15,16). Furthermore, some cGAS may generally be present within the nucleus (17,18), even though cGAS activation is not observed under normal growth. cGAS mutations that weaken nuclear tethering of cGAS constitutively activate it without the need for exogenous DNA (18), but the structural basis of nuclear tethering and cGAS inhibition remains unclear.

Isolated chromatin (19) or reconstituted nucleosomes (15) can bind cGAS, but stimulate cGAMP synthesis less effectively than naked DNA (15,19,20). Furthermore, cGAS has higher affinity for reconstituted nucleosomes than for DNA, and nucleosomes competitively inhibit DNA-dependent cGAS activation (15), suggesting that nucleosome binding underlies the inefficient cGAS activation by chromosomes. To monitor nucleosome-dependent suppression under physiological conditions, we used interphase *Xenopus* egg extracts, where exogenously added DNA efficiently assembles into functional chromatin (Fig. 1A and B) (21). When chromatin formation was prevented by depleting histones H3-H4 from the extract (21), exogenously added DNA stimulated cGAMP production following cGAS addition (Fig. 1A and B). In mock-depleted control extracts, after nucleosome assembly, cGAS activity was severely impaired (Fig. 1A and B and fig. S1), indicating that chromatin inhibits cGAS under physiological conditions.

To reveal the mechanism underlying the nucleosome-mediated suppression of cGAS activation, we determined the cryo-electron microscopy (cryo-EM) structure of the complex formed between nucleosome core particles (NCPs) and human cGAS lacking the unstructured N terminus. This construct was chosen since the N terminus induces aggregation and liquid phase separation, which would interfere with structural analysis (22). Native gel electrophoresis confirmed that, similar to nucleosomes with linker DNA, cGAS binds to NCPs with higher affinity than to naked DNA (Fig. 1C). Cryo-EM visualization of these cGAS-NCP complexes showed that the majority of NCP-like particles are bridged by cGAS-like particles to form stacks (fig. S2). To obtain higher resolution EM maps, we employed GraFix (23). Two major complexes (1 and 2) were isolated and subjected to cryo-EM analysis (fig. S3A and B). Similar to unfixed samples, most NCP-like particles formed multimers, where cGAS-like particles were seen between NCPs (fig. S3C and D). Consistent with their gel migration, complex 1 and complex 2 were predominantly composed of 2 and 3 NCPs, respectively (fig. S3C and D). We consider this multimeric configuration to represent the major organization of the cGAS-NCP complex, and subsequently focused on complex 1, due to its simpler organization (figs. S4 to S6, table S1). The large majority (86%) of particles in complex 1 that were processed for 3D-classification contained two nucleosomes (fig. S4B). While some of these classes contained one cGAS protomer between two NCPs, suggesting some variability in the possible arrangements, the highest resolution was obtained in the class that contained two cGAS protomers between the two NCPs (fig. S4B).

In the cGAS-NCP complex structure with 3.9 Å resolution (fig. S5), two cGAS monomers bind two NCPs, forming a sandwich-like structure in which the NCPs are intimately associated (Fig. 2A). One cGAS molecule fits well into the cryo-EM map, but the cryo-EM map for the other cGAS molecule is more ambiguous (fig. S6A). A 3.3 Å resolution structure of the resolved cGAS-NCP was generated by a focused refinement after subtraction of the ambiguous cGAS-NCP (figs.

S4 and S5). Although resolution of the catalytic pocket is not high enough to assess its local conformation (fig. S5D and E), it is clear that this cGAS monomer binds to the proximal NCP at the acidic patch on the H2A-H2B dimer surface and DNA around superhelical location (SHL) 5.5 (proximal NCP, Fig. 2B); by binding DNA around SHLs3-4 in the other NCP (distal NCP), it also bridges the two NCPs (Fig. 2, A and C). The ambiguous cGAS monomer may bind to similar NCP surfaces, because cryo-EM densities were observed around nearly symmetric NCP regions (fig. S6C). The ambiguity of this cGAS monomer may reflect its flexibility. Below we will focus our analysis on interactions between the resolved cGAS and the two NCPs.

In previous crystal structures of the cGAS dimer-DNA complex, two cGAS protomers sandwich two DNA fragments, with each cGAS protomer binding one DNA fragment with site A, and the other with site B, which are both essential for cGAS activation (3,4,6,24-27) (fig. S7). Site C contributes to cGAS activation by promoting DNA-mediated oligomerization (3) (fig. S7). Within the cGAS-DNA complex, cGAS dimerization is also important for catalytic activation (4). However, direct interaction of the two cGAS protomers in the cGAS-NCP complex is prevented due to steric hindrance (fig. S8). Furthermore, the configuration of each cGAS-DNA binding site is reorganized in the context of NCP binding in a manner that is incompatible with binding to exogenous DNA.

Although site A is solvent-exposed in the cGAS-NCP complex and does not contact nucleosomal DNA (Fig. 3A, left panel), it is inaccessible to exogenous DNA due to steric clashes with the proximal NCP (Fig. 3A, right panel). The lack of interactions at site A in the NCP complex is consistent with our previous findings that site A mutations do not affect the affinity of cGAS for mononucleosomes nor cGAS association with mitotic chromosomes (15).

Site B is repurposed, with a loop segment binding histones rather than DNA (Fig. 2B). R236, K254, and R255 of the loop do not bind DNA, but directly bind to the acidic patch of the proximal NCP (Fig. 3B), a hotspot for chromatin interactors (28). The side chain density of cGAS R255 is clearly visible, and interacts with residues E61, D90, and E92 of histone H2A (Fig. 3B), forming a classic arginine anchor such as found in Kaposi's sarcoma LANA peptide (fig. S9). As previously indicated (18), this loop is conserved among vertebrate cGAS homologs (fig. S10), but not in the RNA-activated cGAS paralog OAS1 (figs. S10 and 11). In addition, an  $\alpha$ -helix within site B (residues 346-355) is located near the DNA around SHL5.5 of the proximal NCP. K347 and K350 within this  $\alpha$ -helix may interact with the major groove and the backbone of the nucleosomal DNA, respectively (Fig. 3C). The main chain moieties of other site B residues K327, S328, S329, and L354 are located close to R71 of histone H2A, and may stabilize the cGAS-NCP interaction (Fig. 3D). Altogether, key residues of site B essential for DNA-mediated cGAS activation (3,5,25-27) are blocked by the NCP in the cGAS-NCP complex.

cGAS DNA-binding site C (fig. S7) binds DNA of the distal NCP in the cGAS-NCP complex (Fig. 2C).  $\alpha$ -helix residues 273-290 within site C are located near nucleosomal DNA around SHL3 (Fig. 3E). In this  $\alpha$ -helix, the basic residues R281, K282, and K285 may interact with the DNA backbone (Fig. 3E). The KRKR loop (K299, R300, K301, and R302) (3), may also interact with nucleosomal DNA around SHL3 (Fig. 3E). K427, K428, and H429, which form the KKH loop (3), may interact with nucleosomal DNA around SHL4 (Fig. 3F). In this context, site C cannot access DNA in trans outside of the complex. This potentially suppresses liquid-liquid phase separation-mediated enrichment of cGAS to nucleosome-free DNA within chromatin (3, 22). Gel shift analysis shows that while cGAS mutated at these site C basic residues can bind NCPs

to form complexes with discrete sizes, it cannot form large multimers (fig. S12), suggesting that site C is required for cGAS to generate NCP stacks.

To confirm our interpretations of NCP-dependent suppression of cGAS activity, we focused on site B interactions with the acidic patch of the NCP (Fig. 3B), as site C mutations inactivate human cGAS (3). Mutating the acidic patch (ap\*\*; H2A E56T, E61T, E64T, D90S, E91T, E92T and H2B E105T and E113T) abrogated the high affinity interaction between cGAS and the NCP (Fig. 4, A and B; fig. S13A). R255 of cGAS site B, which binds the acidic patch (Fig. 3B), is highly conserved in vertebrates, but is predicted not to be involved in DNA binding (18)(fig. S10). In cells, mutating R255 and the equivalent R241 of mouse cGAS to glutamic acid was reported to weaken the tight nuclear tethering of cGAS (18). To test if R255 is critical for NCP binding, we prepared mutant human cGAS, in which R255 was replaced by glutamic acid (cGAS<sub>R255E</sub>, fig. S13B). Consistent with our structure model, NCP binding of cGAS<sub>R255E</sub> was decreased, whereas DNA binding was largely unaffected (Fig. 4, B-E; fig. S13C). Unlike wildtype cGAS that binds NCPs with higher affinity than naked DNA, cGAS<sub>R255E</sub> did not show such preference (Fig. 4, B to E). Furthermore, while wildtype cGAS bound to H2A-H2B dimers, this interaction was not observed for cGAS<sub>R255E</sub> (Fig. 4F). Similarly, as we showed previously (15), acidic patch mutations in H2A and H2B (ap\*; H2A E56A, E61A, E64A, D90A, E91A, E92A, and H2B E113A) also interfere with cGAS interaction (Fig. 4F). These data indicate that the interaction between R255 of cGAS and the nucleosome acidic patch is crucial for specific binding of cGAS to nucleosomes.

To test if this interaction is important for inhibition of DNA-dependent cGAS activation, we monitored how naked DNA, wildtype NCPs, or ap\*\* NCPs stimulate cGAMP production by wildtype cGAS or cGAS<sub>R255E</sub>. In contrast to the almost complete inhibition of cGAMP production by wildtype NCPs with wildtype cGAS, using either cGAS<sub>R255E</sub> or ap\*\* NCPs increased cGAMP production (Fig. 4G; figs. S14 and S15), supporting the importance of interactions between cGAS and the acidic patch for cGAS inhibition. However, this did not lead to full activation of cGAS (Fig. 4G and fig. S14), likely due to the conformation of nucleosomal DNA, which may not be optimal for cGAS activation. On naked DNA, cGAS makes many contacts with the backbone of more than a full turn of DNA, which is in a straight conformation (3,4,24-27) (fig. S7). In contrast, the curvature of DNA wrapped around the histone octamer may interfere with the structural changes in cGAS required for full catalytic activity (example shown in fig. S16).

The significance of the cGAS-acidic patch interactions for cGAS inhibition was better illustrated when competitive inhibition of naked-DNA stimulated cGAMP production was assessed (Fig. 4G, combinations of DNA and wt/ap\*\* NCPs). While wildtype NCPs were able to competitively inhibit wildtype cGAS activation by an equal amount of naked DNA, ap\*\* NCPs lost this inhibitory activity (Fig. 4G, left). In contrast, cGAS<sub>R255E</sub> was refractory to inhibition by even wildtype NCPs (Fig. 4G, right). Moreover, while wildtype cGAS is suppressed by NCPs with or without the linker DNA, cGAS<sub>R255E</sub> is activated by NCPs with linker DNA but not by NCPs without linker DNA (fig. S17). These findings predict that cGAS<sub>R255E</sub>, which cannot be competitively inhibited by NCPs, is activated by nucleosome-free segments of genomic DNA in cells. Indeed, in HeLa cells expressing cGAS<sub>R255E</sub>, high basal levels of cGAMP have been observed (18). Altogether, these structural, biochemical and cellular analyses support the importance of the interaction between cGAS site B and the nucleosome acidic patch in competitive inhibition of DNA-dependent cGAS activation.

The competitive inhibition by nucleosomes can explain how stimulation of cGAS by chromosomal self-DNA can be prevented, despite the presence of nucleosome-free regions. Our

analysis indicates that NCPs can competitively inhibit cGAS activation by at least four mechanisms (fig. S18). First, DNA-binding at site A is prevented by steric clashes with the proximal NCP. Second, site B is occupied by the acidic patch of the proximal NCP, and therefore inaccessible to exogenous DNA. Third, cGAS dimerization is prevented by steric clashes with the proximal NCP. Fourth, the formation of tandem cGAS-NCP chains via sites B and C would prevent cGAS-DNA oligomerization, which is required for full activation (3,4). However, the fourth mechanism may be species specific, since several site C basic residues that are predicted to contact nucleosomal DNA, such as those in the KRKR and KKH loops, are not highly conserved (3) (fig. S10). As human and mouse cGAS exhibit different enzymatic, DNA-length sensitivity and phase-separation characteristics (3,22), chromatin inhibition of cGAS may also be modified species-specifically. It is likely that diverse mechanisms, such as the expression of H2A variants that lack the acidic patch, regulate the nucleosome-dependent suppression of cGAS.

## References and Notes:

1. A. Ablasser, Z. J. Chen, cGAS in action: Expanding roles in immunity and inflammation. *Science* **363**, 6431 (2019).
2. M. Motwani, S. Pesiridis, K. A. Fitzgerald, DNA sensing by the cGAS-STING pathway in health and disease. *Nat. Rev. Genet.* **20**, 657-674 (2019).
3. W. Xie, L. Lama, C. Adura, D. Tomita, J. F. Glickman, T. Tuschl, D. J. Patel, Human cGAS catalytic domain has an additional DNA-binding interface that enhances enzymatic activity and liquid-phase condensation. *Proc. Natl. Acad. Sci. U. S. A.* **116**, 11946-11955 (2019).
4. X. Li, C. Shu, G. Yi, C. T. Chaton, C. L. Shelton, J. Diao, X. Zuo, C. C. Kao, A. B. Herr, P. Li, Cyclic GMP-AMP synthase is activated by double-stranded DNA-induced oligomerization. *Immunity* **39**, 1019-1031 (2013).
5. R. M. Hooy, J. Sohn, The allosteric activation of cGAS underpins its dynamic signaling landscape. *eLife* **7**, e39984 (2018).
6. P. Gao, M. Ascano, Y. Wu, W. Barchet, B. L. Gaffney, T. Zillinger, A. A. Serganov, Y. Liu, R. A. Jones, G. Hartmann, T. Tuschl, D. J. Patel, Cyclic [G(2',5')pA(3',5')p] is the metazoan second messenger produced by DNA-activated cyclic GMP-AMP synthase. *Cell* **153**, 1094-1107 (2013).
7. H. Ishikawa, G. N. Barber, STING is an endoplasmic reticulum adaptor that facilitates innate immune signalling. *Nature* **455**, 674-678 (2008).
8. L. Sun, J. Wu, F. Du, X. Chen, Z. J. Chen, Cyclic GMP-AMP synthase is a cytosolic DNA sensor that activates the type I interferon pathway. *Science* **339**, 786-791 (2013).
9. J. Wu, L. Sun, X. Chen, F. Du, H. Shi, C. Chen, Z. J. Chen, Cyclic GMP-AMP is an endogenous second messenger in innate immune signaling by cytosolic DNA. *Science* **339**, 826-830 (2013).
10. A. Ablasser, M. Goldeck, T. Cavlar, T. Deimling, G. Witte, I. Röhl, K. P. Hopfner, J. Ludwig, V. Hornung, cGAS produces a 2'-5'-linked cyclic dinucleotide second messenger that activates

STING. *Nature* **498**, 380-384 (2013).

11. K. Kato K, H. Omura, R. Ishitani, O. Nureki, Cyclic GMP-AMP as an endogenous second messenger in innate immune signaling by cytosolic DNA. *Annu. Rev. Biochem.* **86**, 541-566 (2017).
- 5 12. H. Ishikawa, Z. Ma, G. N. Barber, STING regulates intracellular DNA-mediated, type I interferon-dependent innate immunity. *Nature* **461**, 788-792 (2009).
13. M. Gentili, X. Lahaye, F. Nadalin, G. P. F. Nader, E. Puig Lombardi, S. Herve, N.S. De Silva, D. C. Rookhuizen, E. Zueva, C. Goudot, M. Maurin, A. Bochnakian, S. Amigorena, M. Piel, D. Fachinetti, A. Londoño-Vallejo, N. Manel, The N-terminal domain of cGAS determines preferential association with centromeric DNA and innate immune activation in the nucleus. *Cell Rep.* **26**, 2377-2393 (2019).
- 10 14. H. Yang, H. Wang, J. Ren, Q. Chen, Z.J. Chen, cGAS is essential for cellular senescence. *Proc. Natl. Acad. Sci. U. S. A.* **114**, E4612-E4620 (2017).
- 15 15. C. Zierhut, N. Yamaguchi, M. Paredes, J. D. Luo, T. Carroll, H. Funabiki, The cytoplasmic DNA sensor cGAS promotes mitotic cell death. *Cell* **178**, 302-315 (2019).
16. L. Zhong, M.M. Hu, L.J. Bian, Y. Liu, Q. Chen, H.B. Shu, Phosphorylation of cGAS by CDK1 impairs self-DNA sensing in mitosis. *Cell Discov.* **6**, 26 (2020).
17. H. Jiang, X. Xue, S. Panda, A. Kawale, R. M. Hooy, F. Liang, J. Sohn, P. Sung, N. O. Gekara, Chromatin-bound cGAS is an inhibitor of DNA repair and hence accelerates genome destabilization and cell death. *EMBO J.* **38**, e102718 (2019).
- 20 18. H. E. Volkman, S. Cambier, E. E. Gray, D. B. Stetson, Tight nuclear tethering of cGAS is essential for preventing autoreactivity. *eLife* **8**, e47491 (2019).
19. K. J. Mackenzie, P. Carroll, C. A. Martin, O. Murina, A. Fluteau, D.J. Simpson, N. Olova, H. Sutcliffe, J. K. Rainger, A. Leitch, R. T. Osborn, A. P. Wheeler, M. Nowotny, N. Gilbert, T. Chandra, M. A. M. Reijns, A. P. Jackson, cGAS surveillance of micronuclei links genome instability to innate immunity. *Nature* **548**, 461-465 (2017).
- 25 20. X. Lahaye, M. Gentili, A. Silvin, C. Conrad, L. Picard, M. Jouve, E. Zueva, M. Maurin, F. Nadalin, G. J. Knott, B. Zhao, F. Du, M. Rio, J. Amiel, A. H. Fox, P. Li, L. Etienne, C. S. Bond, L. Colleaux, N. Manel, NONO detects the nuclear HIV capsid to promote cGAS-mediated innate immune activation. *Cell* **175**, 488-501 (2018).
- 30 21. C. Zierhut, C. Jenness, H. Kimura, H. Funabiki, Nucleosomal regulation of chromatin composition and nuclear assembly revealed by histone depletion. *Nat. Struct. Mol. Biol.* **21**, 617-625 (2014).
22. M. Du, Z. J. Chen, DNA-induced liquid phase condensation of cGAS activates innate immune signaling. *Science* **361**, 704-709 (2018).
- 35 23. B. Kastner, N. Fischer, M. M. Golas, B. Sander, P. Dube, D. Boehringer, K. Hartmuth, J. Deckert, F. Hauer, E. Wolf, H. Uchtenhagen, H. Urlaub, F. Herzog, J. M. Peters, D. Poerschke, R. Lührmann, H. Stark, GraFix: sample preparation for single-particle electron cryomicroscopy. *Nat. Methods* **5**, 53-55 (2008).
- 40 24. F. Civril, T. Deimling, C. C. de Oliveira Mann, A. Ablasser, M. Moldt, G. Witte, V. Hornung,

- K.P. Hopfner, Structural mechanism of cytosolic DNA sensing by cGAS. *Nature* **498**, 332-337 (2013).
25. X. Zhang, J. Wu, F. Du, H. Xu, L. Sun, Z. Chen, C. A. Brautigam, X. Zhang, Z. J. Chen, The cytosolic DNA sensor cGAS forms an oligomeric complex with DNA and undergoes switch-like conformational changes in the activation loop. *Cell Rep.* **6**, 421-430 (2014).
26. L. Andreeva, B. Hiller, D. Kostrewa, C. Lässig, C. C. de Oliveira Mann, D. Jan Drexler, A. Maiser, M. Gaidt, H. Leonhardt, V. Hornung, K.P. Hopfner, cGAS senses long and HMGB/TFAM-bound U-turn DNA by forming protein-DNA ladders. *Nature* **549**, 394-398 (2017).
27. W. Zhou, A. T. Whiteley, C. C. de Oliveira Mann, B. R. Morehouse, R. P. Nowak, E. S. Fischer, N. S. Gray, J. J. Mekalanos, P. J. Kranzusch, Structure of the human cGAS-DNA complex reveals enhanced control of immune surveillance. *Cell* **174**, 300-311 (2018).
28. A. A. Kalashnikova, M. E. Porter-Goff, U. M. Muthurajan, K. Luger, J. C. Hansen, The role of the nucleosome acidic patch in modulating higher order chromatin structure. *J. R. Soc. Interface* **10**, 20121022 (2013).
29. T. Kujirai, Y. Arimura, R. Fujita, N. Horikoshi, S. Machida, H. Kurumizaka, Methods for Preparing Nucleosomes Containing Histone Variants. *Methods Mol. Biol.* **1832**, 3-20 (2018).
30. D. Vasudevan, E. Y. Chua, C. A. Davey, Crystal structures of nucleosome core particles containing the '601' strong positioning sequence. *J. Mol. Biol.* **403**, 1-10 (2010).
31. Y. Arimura, H. Tachiwana, T. Oda, M. Sato, H. Kurumizaka, Structural analysis of the hexasome, lacking one histone H2A/H2B dimer from the conventional nucleosome. *Biochemistry* **51**, 3302-3309 (2012).
32. P. T. Lowary, J. Widom, New DNA sequence rules for high affinity binding to histone octamer and sequence-directed nucleosome positioning. *J. Mol. Biol.* **276**, 19-42 (1998).
33. D. N. Mastronarde, Automated electron microscope tomography using robust prediction of specimen movements. *J. Struct. Biol.* **152**, 36-51 (2005).
34. S. Q. Zheng, MotionCor2: anisotropic correction of beam-induced motion for improved cryo-electron microscopy. *Nat. Methods* **14**, 331-332 (2017).
35. K. Zhang, Gctf: Real-time CTF determination and correction. *J. Struct. Biol.* **193**, 1-12 (2016).
36. J. Zivanov, T. Nakane, B. O. Forsberg, D. Kimanius, W. J. Hagen, E. Lindahl, S. H. Scheres, New tools for automated high-resolution cryo-EM structure determination in RELION-3. *eLife*. **7**, e42166 (2018).
37. Y.Z. Tan, P.R. Baldwin, J.H. Davis, J.R. Williamson, C.S. Potter, B. Carragher, D. Lyumkis, Addressing preferred specimen orientation in single-particle cryo-EM through tilting. *Nat. Methods*, **14**, 793–796 (2017).
38. E. Ramírez-Aportela, J. L. Vilas, A. Glukhova, R. Melero, P. Conesa, M. Martínez, D. Maluenda, J. Mota, A. Jiménez, R. J. Vargas, Marabini, P. M. Sexton, J. M. Carazo, C. O. S. Sorzano, Automatic local resolution-based sharpening of cryo-EM maps. *Bioinformatics* **36**, 765-772 (2020).
39. J. L. Vilas, J. Gómez-Blanco, P. Conesa, R. Melero, J. Miguel de la Rosa-Trevín, J. Otón, J.

Cuenca, R. Marabini, J. M. Carazo, J. Vargas, C. O. S. Sorzano, MonoRes: Automatic and accurate estimation of local resolution for electron microscopy maps. *Structure* **26**, 337-344 (2018).

- 5 40. J. M. de la Rosa-Trevín, A. Quintana, L. Del Cano, A. Zaldívar, I. Foche, J. Gutiérrez, J. Gómez-Blanco, J. Burguet-Castell, J. Cuenca-Alba, V. Abrishami, J. Vargas, J. Otón, G. Sharov, J. L. Vilas, J. Navas, P. Conesa, M. Kazemi, R. Marabini, C. O. Sorzano, J. M. Carazo, Scipion: A software framework toward integration, reproducibility and validation in 3D electron microscopy. *J. Struct. Biol.* **195**, 93-99 (2016).
- 10 41. D. N. Kim, N. W. Moriarty, S. Kirmizialtin, P. V. Afonine, B. Poon, O. V. Sobolev, P. D. Adams, K. Sanbonmatsu, *Cryo\_fit*: Democratization of flexible fitting for cryo-EM. *J. Struct. Biol.* **208**, 1-6 (2019).
42. P. Emsley, B. Lohkamp, W. G. Scott, K. Cowtan, Features and development of Coot. *Acta Crystallogr. D Biol. Crystallogr.* **66**, 486-501 (2010).
- 15 43. D. Liebschner, P. V. Afonine, M. L. Baker, G. Bunkóczi, V. B. Chen, T. I. Croll, B. Hintze, L. W. Hung, S. Jain, A. J. McCoy, N. W. Moriarty, R. D. Oeffner, B. K. Poon, M. G. Prisant, R. J. Read, J. S. Richardson, D. C. Richardson, M. D. Sammito, O. V. Sobolev, D. H. Stockwell, T. C. Terwilliger, A. G. Urzhumtsev, L. L. Videau, C. J. Williams, P. D. Adams, Macromolecular structure determination using X-rays, neutrons and electrons: recent developments in Phenix. *Acta Crystallogr. D Struct. Biol.* **75**, 861-877 (2019).
- 20 44. C. J. Williams, J. J. Headd, N. W. Moriarty, M. G. Prisant, L. L. Videau, L. N. Deis, V. Verma, D. A. Keedy, B. J. Hintze, V. B. Chen, S. Jain, S. M. Lewis, W. B. 3rd Arendall, J. Snoeyink, P. D. Adams, S. C. Lovell, J. S. Richardson, D. C. Richardson, MolProbity: More and better reference data for improved all-atom structure validation. *Protein Sci.* **27**, 293-315 (2018).
- 25 45. B.A. Barad, N. Echols, R.Y. Wang, Y. Cheng, F., DiMaio, P.D. Adams, J. S. Fraser, EMRinger: side chain-directed model and map validation for 3D cryo-electron microscopy. *Nat. Methods* **12**, 943-946 (2015).
46. E. F. Pettersen, T. D. Goddard, C. C. Huang, G. S. Couch, D.M. Greenblatt, E. C. Meng, T. E. Ferrin, UCSF Chimera--a visualization system for exploratory research and analysis. *J. Comput. Chem.* **25**, 1605-1612 (2004).
- 30 47. A.W. Murray, Cell cycle extracts. *Methods Cell Biol.* **36**, 581-605 (1991).

**Acknowledgments:** We thank Y. Iikura and J. Kato (University of Tokyo) for their assistance, and Y. Arimura for helpful discussions and comments on the manuscript. We also thank M. Kikkawa for cryo-EM data collection: **Funding:** This work was supported in part by JSPS KAKENHI Grant Numbers JP17H01408 [to H.K.], JP18H05534 [to H.K.], JP19K06522 [to Y.T.], JP20K15711 [to T.K.] and JST CREST Grant Number JPMJCR16G1 [to T.K. and H.K.], the Platform Project for Supporting Drug Discovery and Life Science Research (BINDS) from AMED under Grant Number JP20am0101076 [to H.K.], and JP20am0101115j0004 [to M. Kikkawa], and JST ERATO Grant Number JPMJER1901 [to H.K.], and National Institutes of Health Grants R35GM132111 [to H.F.]. **Author contributions:** C.Z., R.K., T.K., and N.U. purified cGAS proteins. T.K. and S.H. prepared the cGAS-nucleosome complex. C.Z, R.K, T.K. S.H. and L.N. performed biochemical analyses. T.K. and Y.T. performed the cryo-EM analysis. T.K., C.Z., H.F.

35  
40

and H.K. conceived and designed the work. T.K., C.Z., R.K., H.F. and H.K. wrote the paper. H.F. and H.K. guided and supervised all of the work. All of the authors discussed the results and commented on the manuscript. **Competing interests:** The authors declare no competing interests. H.F. is affiliated with the Graduate School of Medical Sciences, Weill Cornell Medicine, and the Cell Biology Program, the Sloan Kettering Institute. **Data and materials availability:** The cryo-EM reconstructions and atomic model of the cGAS-nucleosome complex has been deposited in the Electron Microscopy Data Bank and the Protein Data Bank (PDB) under the accession codes: EMD-30267 and PDB ID: 7C0M. All data and materials are available from the corresponding authors upon request.

## Supplementary Materials:

Materials and Methods

Figures S1-S18

Table S1

References (29-47)

**Fig. 1.** cGAS-mediated cGAMP synthesis is inhibited by nucleosomes under physiological conditions. (A) cGAMP synthesis by cGAS in *Xenopus* egg extracts. Interphase extracts depleted for histones H3-H4 ( $\Delta$ H3-H4) or mock-depleted with unspecific antibodies ( $\Delta$ mock) were incubated with exogenously added plasmid DNA and cGAS. After incubation, samples were taken for Western blotting and cGAMP detection by ELISA. (B) Averages (bars), and SEM (error bars) for the indicated extract types. P value derived with unpaired t test. (C) cGAS-nucleosome binding assay. Increasing amounts of cGAS were mixed with either 145 base-pair (bp) DNA, the nucleosome core particle (NCP) containing 145 bp DNA (no linker DNA), 193 bp DNA, or the nucleosome (nuc.) containing 193 bp DNA (24 bp linker DNA). The indicated species were separated by non-denaturing polyacrylamide gel electrophoresis and visualized with ethidium bromide staining. The result was reproduced in another independent experiment.

**Fig. 2.** Cryo-EM structure of the cGAS-nucleosome complex. (A) Cryo-EM density of the cGAS-nucleosome complex with fitted structural model. (B) cGAS DNA-binding site B (cyan) binds the proximal nucleosome through contacts with DNA at SHL5.5 and with the H2A-H2B dimer. (C) cGAS DNA-binding site C (purple) binds the distal nucleosome at SHL3. DNA-binding site A (beige) does not interact with DNA or histones.

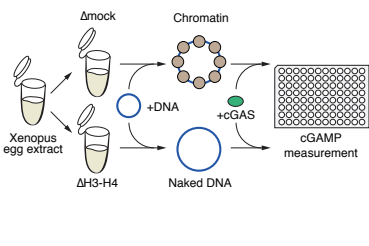
**Fig. 3.** cGAS-nucleosome interactions. (A) Close-up view of cGAS DNA-binding site A in the complex (left). The human cGAS-DNA structure (light gray; PDB ID: 6CT9) and the cGAS-nucleosome structure were superimposed by aligning cGAS (right). Binding of exogenous DNA to site A would cause steric clash with nucleosomal DNA. (B to D) Interactions between the nucleosome and cGAS DNA-binding site B. Close-up views of the cGAS residues, R236, K254, and R255 (B), K347 and K350 (C), L354, K327, S328, and S329 (D), are shown. The focused refined EM-density map after subtraction of the ambiguous cGAS-distal nucleosome (see Methods) was used for representations. (E and F) Interactions between the nucleosome and cGAS

DNA-binding site C. Close-up views of the cGAS  $\alpha$ -helix region containing R281, K282, and K285 (E), KRKR loop containing K299, R300, K301, and R302 (E), and the KKH loop containing K427, K428, and H429 (F) are presented. The EM-density map of the overall structure of the cGAS-nucleosome complex was used for representation. cGAS DNA-binding sites are colored as in Fig. 2.

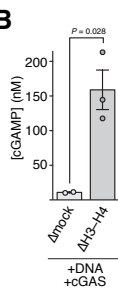
**Fig. 4.** The acidic patch on the nucleosome, and Arg255 of cGAS are required for high affinity association between nucleosomes and cGAS, and for competitive inhibition of cGAS by nucleosomes. (A and B) Quantitative gel shift analysis of the binding affinity between cGAS and naked DNA, or the indicated nucleosomes (wt: wildtype, ap<sup>\*\*</sup>: acidic patch mutated). See fig. S13A for example gels. Data represent mean and SEM of 4 independent experiments. 145 bp naked DNA or NCPs containing 145 bp of DNA were used. (C to E) Quantitative gel shift analysis of the binding affinity between naked DNA, or wt nucleosomes, and the indicated cGAS. Note that C and D are different representations of the same experiments. See fig. S13C for example gels. Data represent mean and SEM of 3 independent experiments. 145 bp naked DNA or NCPs containing 145 bp of DNA were used. (F) Analysis of the interaction between cGAS (wt or R255E) and either wildtype (wt) Hexa-histidine tagged (His<sub>6</sub>)-H2A–H2B dimers or acidic patch mutated (ap<sup>\*</sup>) His<sub>6</sub>-H2A–H2B dimers. cGAS, histones and talon beads were mixed, incubated and collected on a magnet. After washing, bound proteins were separated by gel electrophoresis and visualized with coomassie brilliant blue (CBB). Equal fractions of inputs and pull downs were loaded. Results were confirmed in two additional independent experiments. (G) Quantifications of catalytic activity of the indicated cGAS version with naked DNA, wildtype (wt) NCPs, or acidic patch mutated (ap<sup>\*\*</sup>) NCPs in vitro. Averages (bars) and SEM (error bars) of three experiments (dots) are shown. Naked DNA and NCPs were 145 bp and used at 230 nM each.

# Figure 1

## A



## B



## C

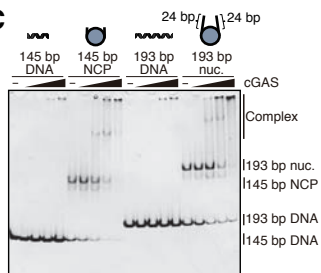


# Figure 2

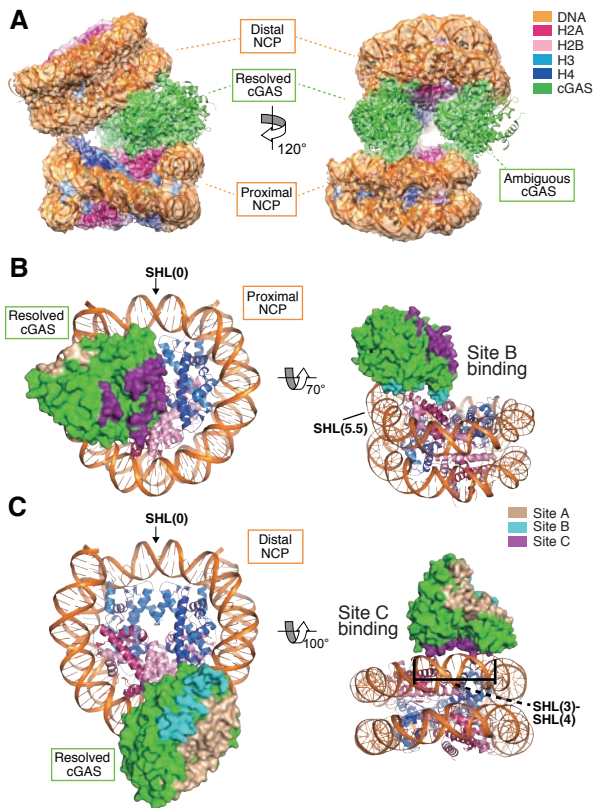
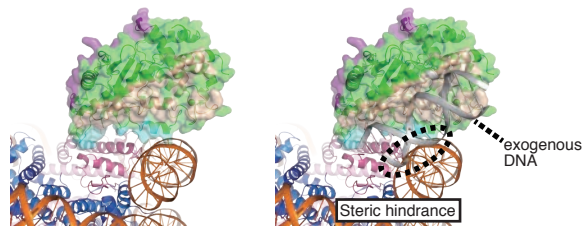
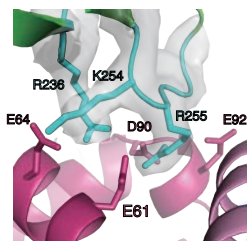


# Figure 3

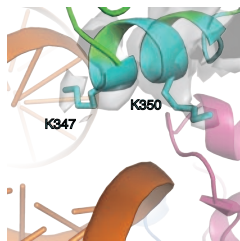
A



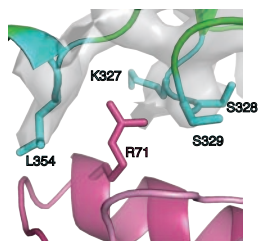
B



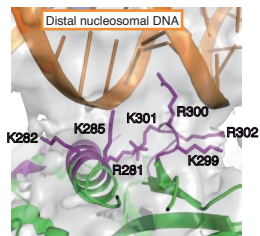
C



D



E



F

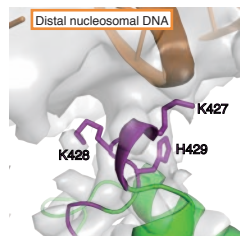
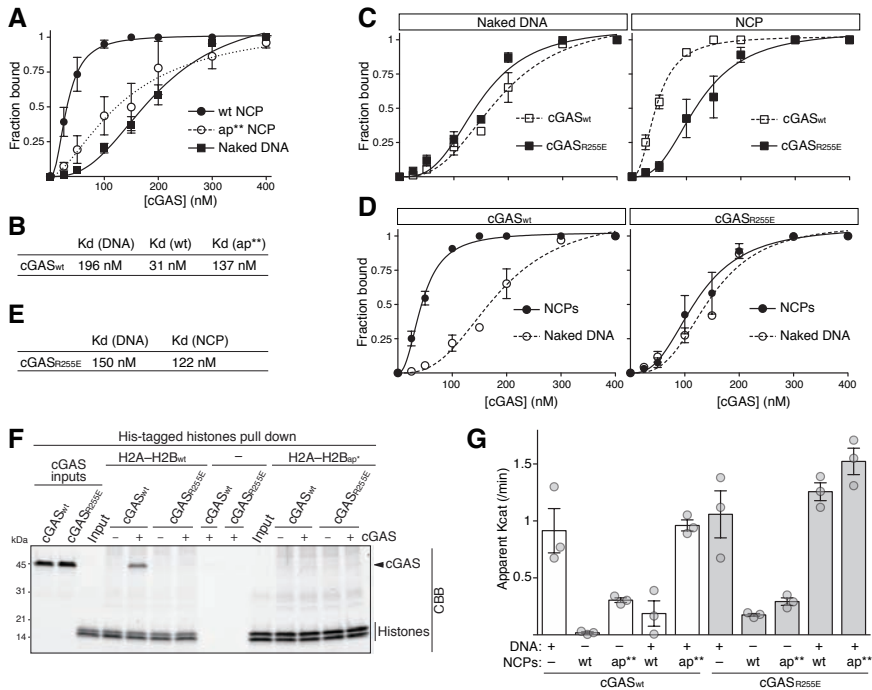


# Figure 4



## Structural basis for the inhibition of cGAS by nucleosomes

**Authors:** Tomoya Kujirai<sup>1</sup>†, Christian Zierhut<sup>2,5</sup>†, Yoshimasa Takizawa<sup>1</sup>, Ryan Kim<sup>2</sup>, Lumi Negishi<sup>1</sup>, Nobuki Uruma<sup>1,3</sup>, Seiya Hirai<sup>1,4</sup>, Hironori Funabiki<sup>2\*</sup>, Hitoshi Kurumizaka<sup>1,3,4\*</sup>

### Affiliations:

<sup>1</sup> Laboratory of Chromatin Structure and Function, Institute for Quantitative Biosciences, The University of Tokyo, 1-1-1 Yayoi, Bunkyo-ku, Tokyo 113-0032, Japan.

<sup>2</sup> Laboratory of Chromosome and Cell Biology, The Rockefeller University, New York, NY 10065, USA

<sup>3</sup> Graduate School of Advanced Science and Engineering, Waseda University, 2-2 Wakamatsucho, Shinjuku-ku, Tokyo 162-8480, Japan.

<sup>4</sup> Department of Biological Sciences, Graduate School of Science, The University of Tokyo, 1-1-1 Yayoi, Bunkyo-ku, Tokyo 113-0032, Japan.

<sup>5</sup> Present address: Division of Cancer Biology, The Institute of Cancer Research, London, SW3 6JB, UK

\*Correspondence to: Hironori Funabiki (e-mail: funabih@rockefeller.edu) or Hitoshi Kurumizaka (e-mail: kurumizaka@iqb.u-tokyo.ac.jp)

†These authors contributed equally to this work.

### Supplementary Materials:

Materials and Methods

Figures S1-S18

Table S1

References (29-47)

## Materials and Methods

### Protein preparation

Recombinant histone proteins including the acidic patch mutant H2A (E56T, E61T, E64T, D90S, E91T, and E92T: ap\*\* H2A) and H2B (E105T and E113T: ap\*\* H2B) used in Fig. 4A, B and G were prepared as described previously (29). Ap\* H2A and H2B for Fig. 4F were H2A (E56A, E61A, E64A, D90A, E91A, and E92A) and H2B (E113A). We chose ap\* mutations to repeat our published data (15), while we used ap\*\* mutations to obtain a stable NCP. Briefly, histone proteins H2A, H2B, H3.1, and H4 were expressed as hexa-histidine (His<sub>6</sub>) tagged proteins in *Escherichia coli* cells, and were purified by Ni-NTA column chromatography (Qiagen) under denaturing condition. After His<sub>6</sub> tag cleavage using thrombin protease (Wako), the resulting histone proteins were further purified by MonoS cation exchange column chromatography (GE healthcare). The purified histone proteins were lyophilized and stored at 4°C.

Recombinant N-terminal truncated human wildtype and mutant cGAS (R255E, K300E\_K301E, and R281A\_K282A\_K285A\_K299A\_R300A\_K301A\_R302A\_K427A\_K428A\_H429A) proteins (151-522 a.a.) were prepared as described previously (15). Briefly, the MBP-cGAS-His<sub>6</sub> proteins were expressed in *E. coli* cells. The cGAS proteins were enriched on Amylose resin, and were eluted by cleavage of both MBP-tag and His<sub>6</sub>-tag using TEV protease. The resulting cGAS proteins were purified by Heparin column chromatography, followed by gel filtration column chromatography with Superdex 200. The purified cGAS proteins were flash-frozen in liquid nitrogen and stored at -80 °C.

### Nucleosome reconstitution

Histone octamers were reconstituted with purified H2A (or ap\*\* H2A), H2B (or ap\*\* H2B), H3, and H4 as described previously (29). 145 base-pair (bp) (30), 193 bp (31) and 200 bp (21) Widom 601 DNA (32) were prepared as described previously (31). Nucleosomes containing the 145 bp (NCP), 193 bp, or 200 bp Widom 601 DNA were reconstituted by the salt dialysis method, and either used directly (fig. S17) or purified by non-denaturing electrophoresis using a Prep Cell apparatus (Bio-Rad) as described previously (all other experiments) (29). The purified nucleosomes were dialyzed in 20 mM Tris-Cl buffer (pH7.5) containing 1 mM DTT and 5 % glycerol. The resulting nucleosomes were flash-frozen in liquid nitrogen and stored at -80 °C.

### Preparation of the cGAS-NCP complex for cryo-EM

For the non-crosslinked cGAS-NCP complex, the cGAS-NCP binding reaction was performed by mixing the NCP (0.2 μM) and cGAS (0.6 μM) in 1 mL of reaction solution (10 mM Tris-Cl (pH 7.5), 300 mM NaCl, and 1.2 mM DTT) at 37°C for 30 min. The reaction mixture was fractionated by sucrose gradient ultracentrifugation. The gradient solution was prepared using the Gradient Master instrument (SKB) using low sucrose concentration solution (20 mM Tris-Cl (pH7.5), 300 mM NaCl, 1 mM DTT, and 10 % sucrose) and high sucrose concentration solution (20 mM Tris-Cl (pH7.5), 300 mM NaCl, 1 mM DTT, 30 % sucrose). The reaction mixture was loaded on the top of the gradient solution. The sample was centrifuged at 27,000 rpm at 4 °C for 16 h using a Beckman SW41 rotor. After centrifugation, 750 μL fractions were taken from the top of the gradient, and the fractions were analyzed by native polyacrylamide gel electrophoresis (PAGE). Fractions containing cGAS-NCP complexes were

then collected, and were desalted using a PD-10 column (GE healthcare) with an elution buffer containing 20 mM Tris-Cl (pH 7.5) and 1 mM DTT. The resulting sample was filtered using Amicon Ultra 30K (Merck Millipore). The DNA concentration of the cGAS-NCP complex plunge frozen for cryo-EM was 170  $\mu\text{g}/\text{mL}$ .

The concentrated sample was applied to Quantifoil grids (Cu, R1.2/1.3. 200 mesh) glow discharged for 1 min by a PIB-10 ION Bombarder (Vacuum Device Inc.). The sample was plunge frozen using a vitrobot mark IV (Thermo Fisher Scientific) at 5 °C and 100 % humidity.

For the preparation of cGAS-NCP complexes crosslinked for single particle analysis, the cGAS-NCP binding reaction was performed by mixing NCP (0.2  $\mu\text{M}$ ) and cGAS (0.3  $\mu\text{M}$ ) in 2 mL of reaction solution (28 mM Tris-Cl (pH 7.5), 55 mM NaCl, 1.3 mM DTT, and 1% glycerol) at 37 °C for 30 min. To stabilize and purify the cGAS-NCP complex, the reaction mixture was fractionated by the GraFix method (23). Gradient solutions were prepared using low sucrose concentration solution (10 mM HEPES-NaOH (pH 7.5), 20 mM NaCl, 1 mM DTT, and 5% sucrose) and high sucrose concentration solution (10 mM HEPES-NaOH (pH 7.5), 20 mM NaCl, 1 mM DTT, 20 % sucrose, and 4 % formaldehyde [diluted from paraformaldehyde solution, Electron Microscopy Sciences, 15710] ). One-fourth of the reaction mixture was loaded on the top of the gradient solution. The sample was centrifuged at 27,000 rpm at 4 °C for 16 h using a Beckman SW41 rotor. After centrifugation, 620  $\mu\text{L}$  fractions were taken from the top of the gradient, and the fractions were analyzed by native-PAGE (fig. S3A). Fractions containing cGAS-NCP complexes 1 and 2 were then separately collected (fig. S3B). The cGAS-NCP complex samples were desalted using a PD-10 column (GE healthcare) with an elution buffer containing 20 mM Tris-Cl (pH 7.5) and 1 mM DTT. The resulting samples were concentrated using Amicon Ultra 50K (Merck Millipore). The DNA concentrations of the cGAS-NCP complexes 1 and 2 plunge frozen for cryo-EM were 61.2  $\mu\text{g}/\text{mL}$  and 24.9  $\mu\text{g}/\text{mL}$ , respectively.

The concentrated samples were applied to Quantifoil grids (Cu, R1.2/1.3. 200 mesh) glow discharged for 1 min by a PIB-10 ION Bombarder (Vacuum Device Inc.). The samples were plunge frozen using a vitrobot mark IV (Thermo Fisher Scientific) at 16 °C and 100 % humidity.

### Cryo-electron microscopy and image processing

For the cGAS-NCP complex 1, cryo-EM images were collected on a Krios G3i cryo-electron microscope (Thermo Fisher Scientific) equipped with K3 BioQuantum (GATAN) with a slit width of 25 eV using SerialEM software (33), operated at 300 kV with a pixel size of 1.05 Å. 7066 movies of the cGAS-NCP complex were recorded. Each movie was fractionated to 40 frames with a total dose of 64  $\text{e}/\text{Å}^2$ . Movie frames were aligned and dose-weighted with MotionCor2 (34). The contrast transfer function was estimated by Gctf (35). Particles were picked automatically with a boxsize of 250 x 250 pixels, picking threshold of 0.1, and minimum inter-particle distance of 130 Å using 2D class averages generated from reference-free auto-picked particles based on Laplacian of Gaussian filter as a reference, and bad particles were removed by 2D classification using RELION3.0 (36). The following processes were performed using RELION3.1 beta. Initial model was prepared using SGD-based initial model generation, followed by 3D classification. The class containing two resolved NCPs was selected and particles were subjected to CTF refinement and bayesian polishing. Further particle selection was performed by 2D classification, and CTF refinement was performed again. The resulting map was postprocessed with a mask covering the overall structure of the cGAS-NCP complex. The resolution of the final maps was 3.9 Å as estimated by the gold standard Fourier shell

correlation (FSC) = 0.143. The local resolution was estimated using RELION local resolution estimation. The 3D FSC curve was calculated with Remote 3DFSC Processing Server (37)(<https://3dfsc.salk.edu/upload/>).

To visualize cGAS-NCP interactions in DNA-binding site B, the density of the ambiguous cGAS and the distal NCP was subtracted from the overall cGAS-NCP complex. CTF refinement was performed and the refined map was sharpened by Localdeblur (38) using the local resolution map estimated by MonoRes (39) in SCIPION framework (40). The resolution of the final map of the resolved cGAS-proximal NCP was 3.3Å as estimated by the gold standard FSC = 0.143.

For the cryo-EM observation of complex 2 and the cGAS-NCP complex without fixation, cryo-EM images were collected by a Talos Arctica G2 cryo-electron microscope (Thermo Fisher Scientific) equipped with K2 BioQuantum (GATAN) with a slit width of 25 eV, operated at 200 kV with a pixel size of 1.32 Å.

### Model building

The atomic model of the cGAS-NCP complex was built based on the crystal structures of the *Xenopus laevis* nucleosome containing the Widom 601 positioning sequence (PDB ID: 3LZ0) (30), and the human cGAS apo form (PDB ID: 4LEV) (4). The NCP structure was fitted with Cryofit (41) against the subtracted and refined map. Then, the cGAS apo form structure was also fitted and edited manually with COOT (42), followed by refinement using phenix.real\_space\_refine (43), against the subtracted and refined map. The amino acid residues of the histones were adjusted to human histones, and selenomethionine residues of the cGAS apo form structure were replaced by methionine. Since the cGAS region interacting with the nucleosomal acidic patch is well-resolved (fig. S5D), the atomic model of cGAS was edited mainly around this region. The atomic model of the overall cGAS-NCP complex was generated by fitting the coordinates based on the subtracted and refined map into the resolved cGAS-NCP part and the ambiguous cGAS-distal NCP part with manual adjustments. Although the density of the ambiguous cGAS part is not well resolved in the overall structure of the cGAS-NCP complex (fig. S6A), the focused refined ambiguous cGAS-distal NCP map showed clear density of cGAS in the ambiguous cGAS part, and the coordinates of cGAS fitted the density of ambiguous cGAS part well (fig. S6B). The final structure was evaluated with the MolProbity (44) and EMRinger (45) programs (Table S1). All structural figures were prepared using UCSF Chimera (46) and PyMOL (Schrödinger; <http://www.pymol.org>).

### Western blotting

Samples were separated using reducing SDS-PAGE and transferred to nitrocellulose membranes. H3 was detected with abcam ab1791 (1 µg/mL); α-tubulin was detected with Sigma T9026 (1:20,000 dilution). Secondary antibodies (IRDye 800CW and 680LT conjugated, LI-COR Biosciences) were used at 50 ng/mL each and detected on an Odyssey infrared imaging system (LI-COR Biosciences).

### Xenopus egg extracts

CSF (cytostatic factor) arrested *Xenopus laevis* egg extracts were prepared as described previously (47). Depletion of histones H3 and H4 was carried out with antibodies recognizing the N-terminally acetylated version of H4 (K12 acetylation) using methods we previously established (21). Control extracts were generated by mock-treatment with an unspecific antibody

of the same isotype, as described previously (21). Work with *X. laevis* was according to a protocol approved by The Rockefeller University Institutional Animal Care and Use Committee. Frogs were obtained from NASCO (cat no. LM00535MX).

#### cGAS activity assays in egg extract

H3–H4 depleted egg extract or mock-depleted extract was mixed with circular pBlueScript at 20 ng/μL and released into interphase by addition of CaCl<sub>2</sub> to 0.3 mM. Egg extracts were incubated for 60 min at 21 °C before cGAS was added to 1 μM final concentration from 20 μM stock in sperm dilution buffer (SDB, 5 mM HEPES, 100 mM KCl, 1 mM MgCl<sub>2</sub>, and 150 mM sucrose, pH 8). After 30 min incubation at 21 °C, a part of the sample was taken for Western blotting (1:20 dilution in 1x reducing SDS sample buffer). The rest of the sample was snap-frozen in liquid nitrogen and stored at -80 °C until use for cGAMP concentration measurement.

#### 2',3'-cGAMP concentration measurements

To measure cGAMP levels, we used the 2',3'-Cyclic GAMP ELISA Kit (Arbor Assays # K067-H1) according to the manufacturer's instructions. Optical density at 450 nm was measured using a Synergy NEO Microplate Reader (BioTek) and adjusted for non-specific binding. Using a Four Parameter Logistic Regression model fitted with cGAMP standards (0.082 to 20 nM with 2.5-fold increase), cGAMP concentrations of the samples were determined after adjusting for dilutions. Samples were diluted 1:250 in assay buffer.

#### Nucleosome, NCP, and naked DNA binding assays

For the gel shift assays of Fig. 4A-E; fig. S12D and S13, 20 nM of either the nucleosome with 24 base-pair linker DNAs, NCPs without linker DNA, or naked DNA was incubated with recombinant cGAS at 25, 50, 100, 150, 200, 300, and 400 nM concentrations in a final volume of 15 μL binding buffer (10 mM Tris-Cl (pH 7 at 22°C), 1 mM EDTA, 0.2 M sucrose, 80 mM NaCl, 5 mM 2-mecaptoethanol, and 0.01% Triton X-100) for 1 h at room temperature. Products were separated on a native 5% polyacrylamide gel with 0.5x TBE as the running buffer. Gels were stained using SYTO-60 DNA stain (Thermo Fisher Scientific). The disappearance of the band corresponding to either naked DNA or NCPs was quantified using ImageJ. This was used to create the binding curves and the corresponding binding affinity was determined using non-linear regression analysis (assuming specific one site binding) on GraphPad Prism (v. 5.0a). Acidic patch mutated NCPs (ap\*\*) were H2A (E56T, E61T, E64T, D90S, E91T, and E92T) and H2B (E105T and E113T).

For the gel shift assays of Fig. 1C and fig. S12B, 100 nM of either the nucleosome with 24 base-pair linker DNAs, NCPs without linker DNA, or naked DNA (145 bp) was incubated with recombinant cGAS at 100, 200, 300, and 400 nM (Fig. 1C) or 150, 225, 300, 450, 675, and 900 nM (fig. S12B) concentrations in a final volume of 10 μL binding buffer (30 mM Tris-Cl (pH 7.5), 90 mM NaCl, 0.5 mM DTT, and 1 % glycerol) for 30 min at 37 °C. Products were separated on a native 4 or 5% polyacrylamide gel with 0.5x TBE as the running buffer. Gels were stained using ethidium bromide.

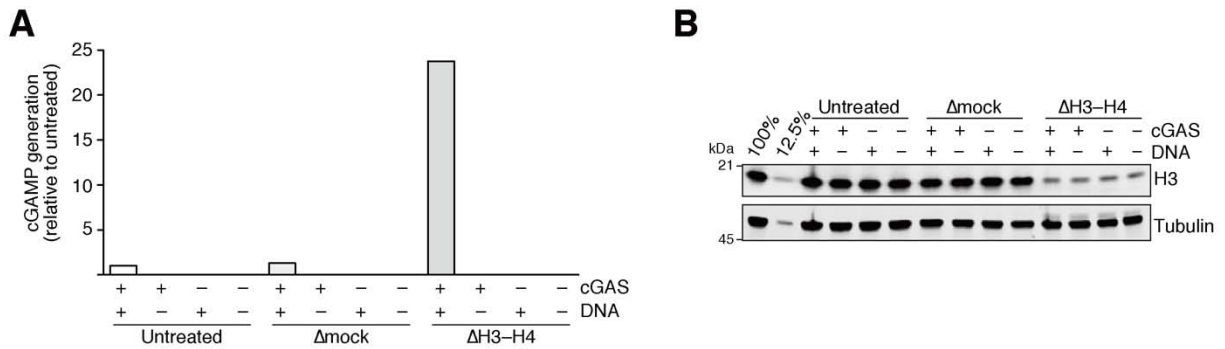
#### cGAMP synthesis assays with reconstituted cGAS, NCPs and nucleosomes with linker DNA

1 μM cGAS was incubated with 230 nM of NCPs (147 bp DNA), 147 bp 601 fragment naked DNA, or combinations thereof for 30 min at 22 °C in reaction buffer (20 mM Tris-Cl (pH

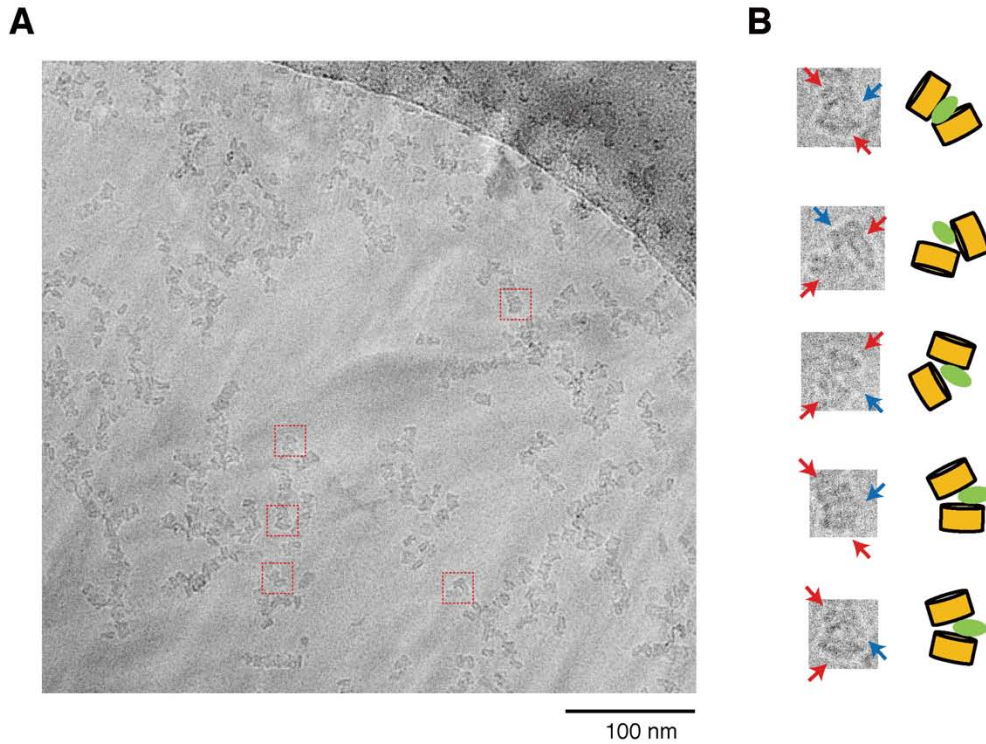
7.5 at 22 °C), 75 mM NaCl, 1 mM DTT, and 6 mM MgCl<sub>2</sub>). For the experiment in fig. S17, 147 bp naked DNA/NCPs at 230 nM were compared to 200 bp naked DNA/nucleosomes at 170 nM to keep the total mass of DNA in each reaction the same. ATP and GTP were then added to a final concentration of 1 mM each, followed by incubation at 37 °C. For competition experiments, reactions contained both naked DNA and NCPs at 230 nM each. 2 μL samples were taken at 10, 20, and 30 min, diluted in 200 μL dilution buffer (20 mM Tris-Cl (pH 7.5 at 22 °C), 75 mM NaCl, 10 mM MgCl<sub>2</sub>) containing 5 U of calf intestinal phosphatase (New England Biolabs), and incubated at 37°C for 30 min. Samples were stored at -80°C until use. After thawing on ice, cGAMP concentrations of each time point were measured using the cGAMP ELISA kit (see above). Samples were diluted 1:50 in assay buffer. Since concentrations of DNA, GTP and ATP under these conditions are high enough for the observed initial velocity to resemble  $V_{\max}$  (see fig. S15 for examples of DNA titration and GTP titration; see *ref. 27* for example of ATP titration), the resulting values were used to determine the initial reaction velocity through linear regression analysis, which was used to determine the  $K_{\text{cat}}$  value of each reaction. Note that due to the fact that cGAS oligomerizes on DNA, and it is unknown if there is cooperativity between the cGAS subunits, the derived  $K_{\text{cat}}$  will only be an approximation (as indicated by the term “apparent  $K_{\text{cat}}$ ”).

#### H2A–H2B binding assay

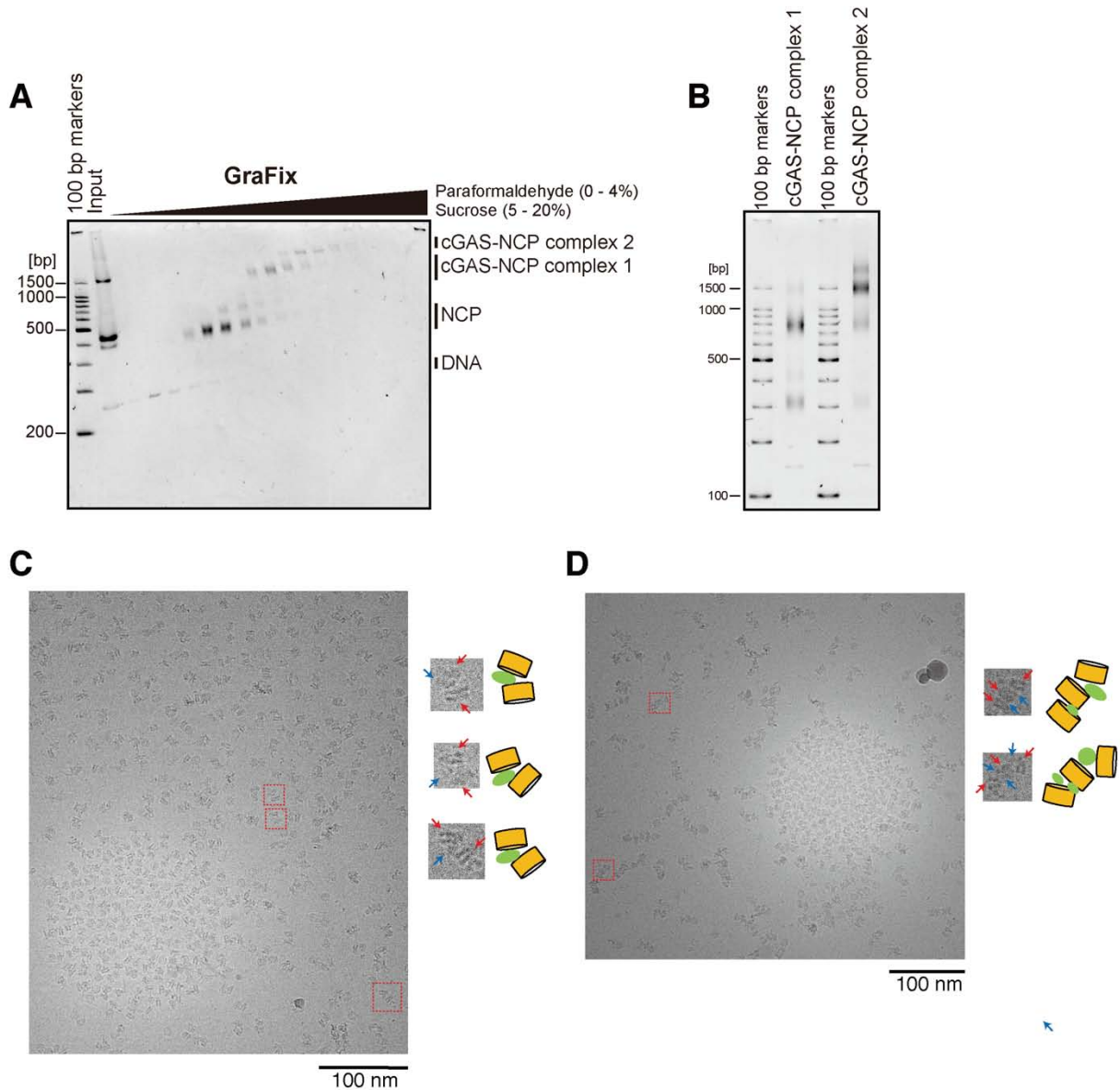
His<sub>6</sub>-tagged H2A–H2B dimers were prepared as previously described (15). With minor modifications, binding assays followed our previous method (15). Briefly, His<sub>6</sub>-H2A–H2B dimers and cGAS were mixed at a final concentration of 100 nM each in binding buffer (20 mM Tris-Cl (pH 8 at 4 °C), 120 mM NaCl, 60 mM imidazole, 0.3 % Tween-20, and 0.01 μg/μL BSA). 200 μL of this mixture was added to 5 μL Dynabeads Talon (Thermo Fisher) and incubated with agitation in a Thermomixer (Eppendorf) at 8 °C for 1 h. Supernatant was removed, and beads were washed three times with binding buffer without BSA. Bound proteins were eluted by incubation with 2x reducing SDS sample buffer (125 mM Tris-Cl (pH 6.8 at 22 °C), 2 % SDS, and 0.7 M 2-mercaptoethanol). Proteins were separated by reducing SDS-PAGE and visualized using GelCode Blue stain (Thermo Fisher Scientific).



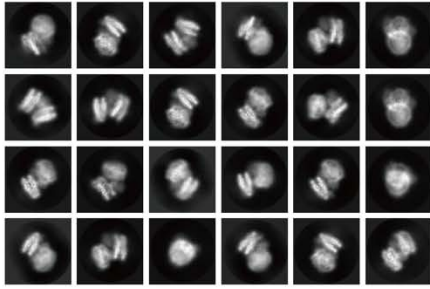
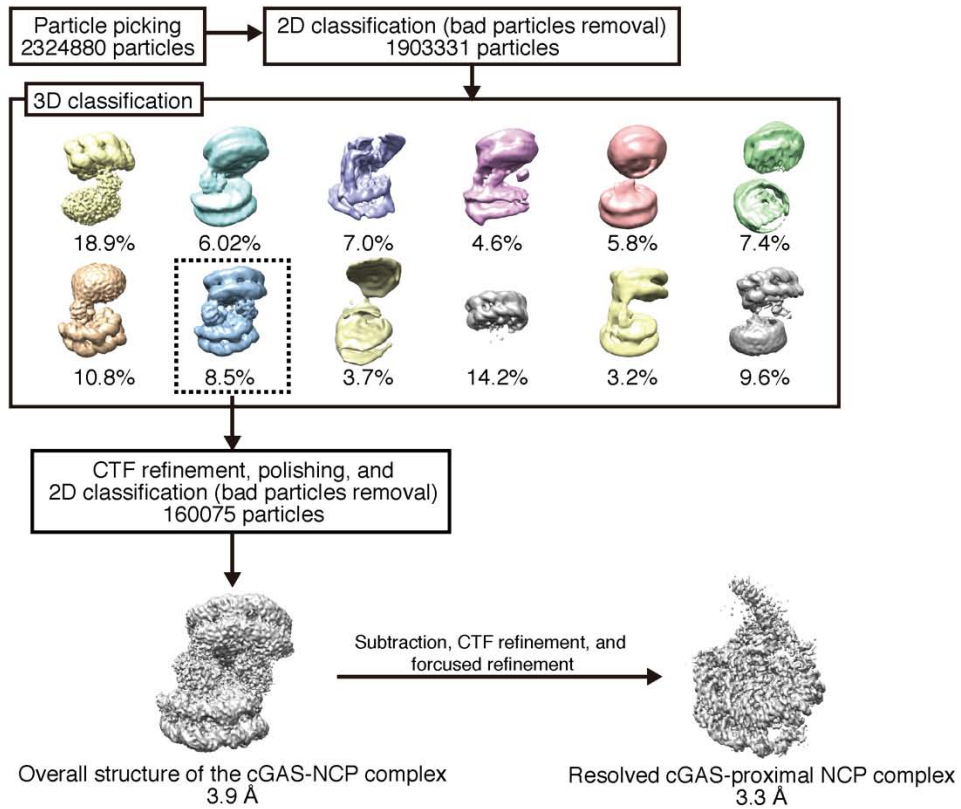
**Fig. S1. Nucleosomes inhibit cGAMP synthesis by cGAS under physiological conditions.** (A and B) Egg extract was either untreated, treated with anti H4K12ac antibody to deplete histones H3 and H4 ( $\Delta$ H3-H4), or mock-depleted with unspecific antibody ( $\Delta$ mock). Interphase extracts of the indicated type were then incubated with pBluescript at 20 ng/ $\mu$ L or buffer for 60 min, following which buffer or cGAS was added to 1  $\mu$ M. After 30 min, samples were taken for Western blotting and cGAMP detection using the cGAMP ELISA kit from Arbor Assays. (A) cGAMP levels. (B) Western blot analysis to confirm histone depletion. 100 %; 12.5 %, samples of diluted extract to determine histone depletion levels.



**Fig. S2. Cryo-EM micrograph without fixation. (A)** A representative micrograph of the cGAS-NCP complex without crosslinking collected with a Talos Arctica G2 cryo-electron microscope. The NCP-like particles form stacks. **(B)** Enlarged images of NCP-like particles bridged with cGAS-like particles. The particles encircled by the dotted square in panel (A) are enlarged and presented. NCPs and cGAS are indicated with red and blue arrows, respectively. Cartoon images corresponding to the cGAS (green circles) -NCP (orange cylinders) complex are also presented.



**Fig. S3 GraFix overview, complexes 1 and 2, and corresponding micrographs.** (A) Fractions separated by GraFix (see Materials and Methods) were analyzed by native-PAGE and ethidium bromide staining. (B) The purified complexes 1 and 2 were analyzed by native-PAGE and ethidium bromide staining. (C) A representative micrograph of complex 1 collected with a Krios G3i cryo-electron microscope. Enlarged images (dotted squares in the micrograph) show examples of NCP-like particles bridged by cGAS-like particles, and are presented with cartoon images as shown in fig. S2. (D) A representative micrograph of complex 2 collected with a Talos Arctica G2 cryo-electron microscope. The particles encircled by the dotted square in the micrograph are enlarged and presented with cartoon images as shown in fig. S2.

**A****B**

**Fig. S4. Cryo-EM data collection and image processing.** (A) Representative 2D classes of the cGAS-NCP complex. (B) Workflow of image processing.

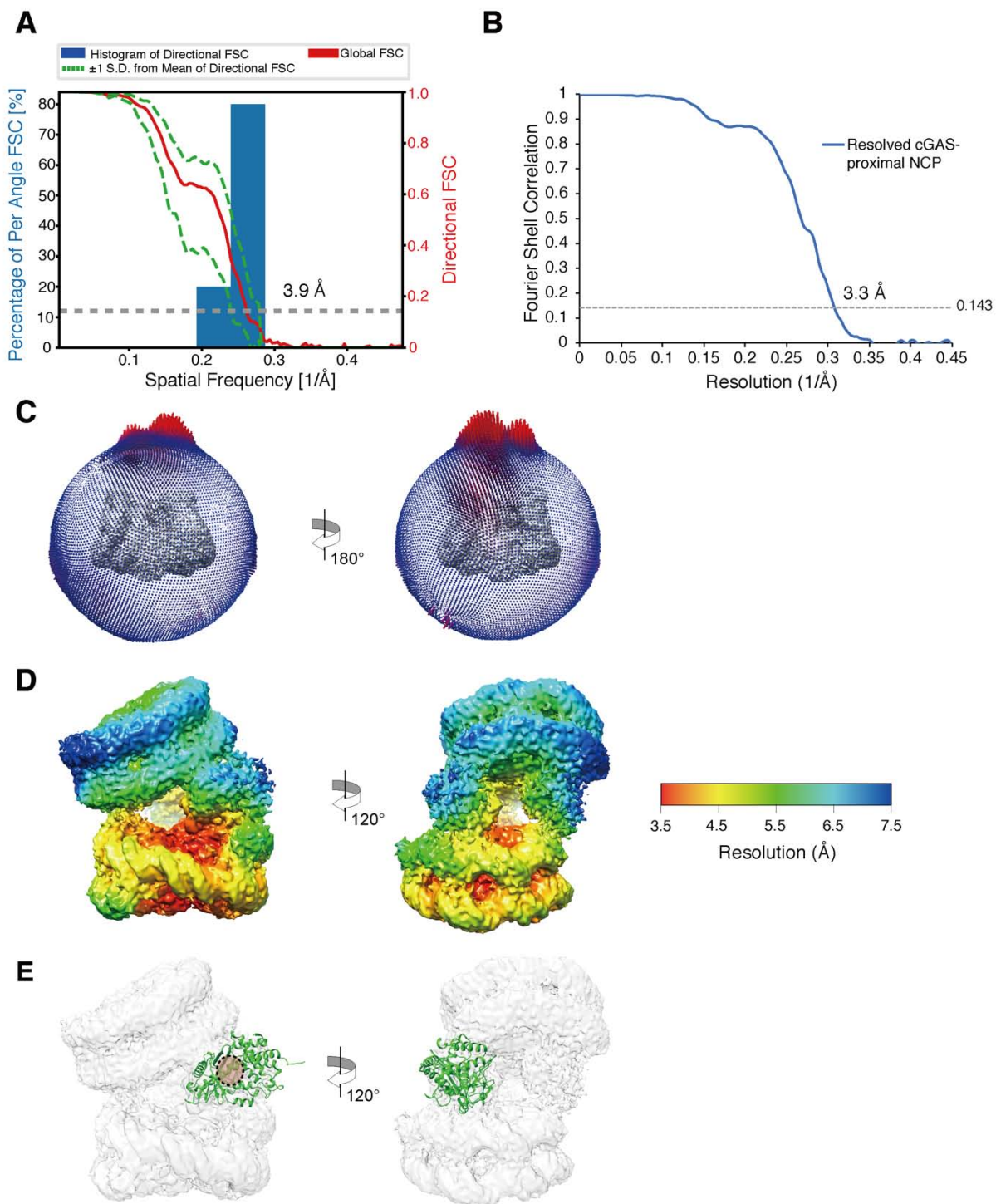


**Fig. S5. Quality of the cGAS-NCP structure.** (A) 3D Fourier shell correlation (FSC) curve for the overall structure of the cGAS-NCP complex. The resolution of the overall structure of the cGAS-NCP complex was estimated to be 3.9  $\text{\AA}$  by an FSC = 0.143. Sphericity is 0.853, indicating that there is no strong anisotropy in the structure. (B) FSC curve for the resolved cGAS-proximal NCP. The resolution of the structure of the resolved cGAS-proximal NCP was estimated to be 3.3  $\text{\AA}$  by an FSC = 0.143. (C) Euler angular distribution of the overall structure

of the cGAS-NCP complex. **(D)** Local resolution map of the overall structure of the cGAS-NCP complex. **(E)** The cryo-EM map of the cGAS-NCP complex fitted with the crystal structure of human cGAS apo form (green; PDB ID: 4LEV). The position of the catalytic pocket is indicated with a dotted circle. Note that the resolved cGAS structure near the nucleosomal acidic patch is well defined but the regions including the cGAS catalytic pocket are ambiguous, although the overall cGAS crystal structure is generally fitted well to the cryo-EM map (also see fig. S6).

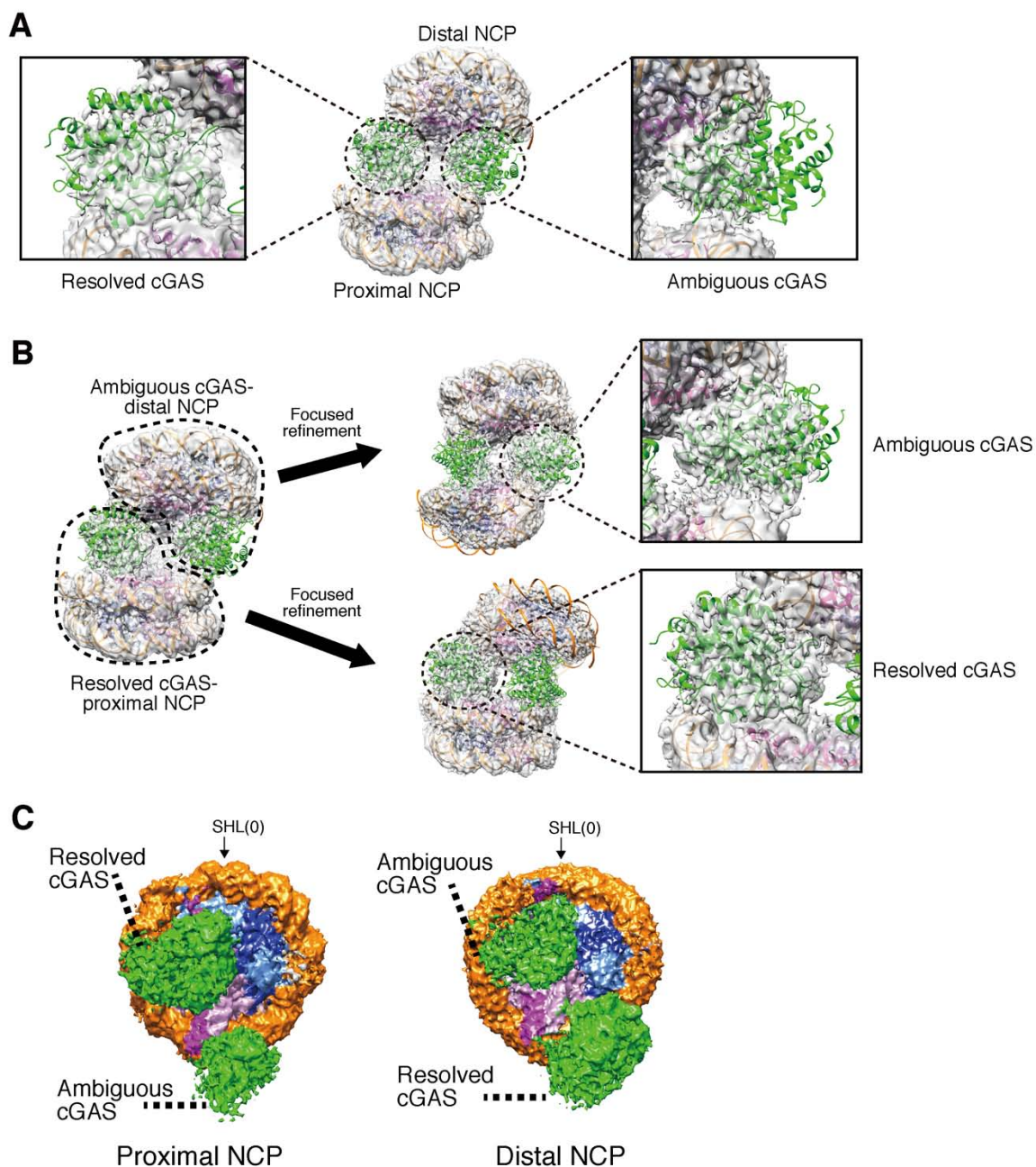


**Fig. S6. Cryo-EM density of the cGAS-NCP complex.** (A) Density of the cGAS-NCP complex. Resolved and ambiguous cGAS density maps without focused refinement are presented within the left and right panel, respectively. (B) The focused, refined maps of the resolved cGAS-proximal NCP complex and of the ambiguous cGAS-distal NCP were calculated. Each atomic model of cGAS fits well into the refined maps. (C) The proximal NCP with the resolved and ambiguous cGAS molecules, and the distal NCP with the resolved and ambiguous cGAS molecules are shown. Both cGAS molecules bind around SHL(5.5) and SHL(3-4).

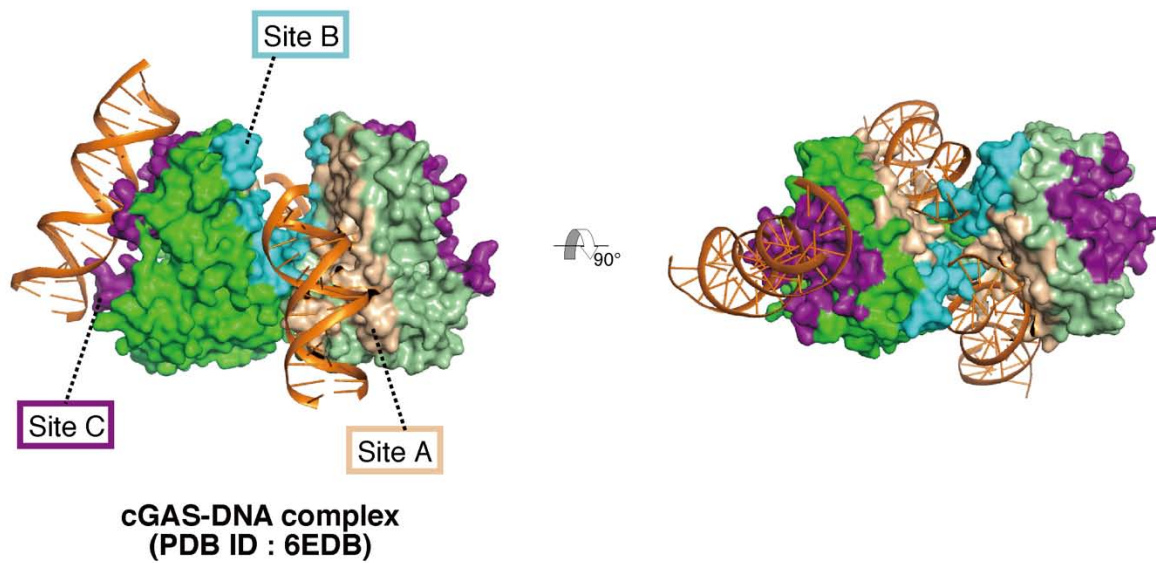


**Fig. S7. cGAS DNA-binding sites.** The human cGAS dimer-DNA complex (PDB ID: 6EDB). cGAS protomers are colored green and pale green. The DNA binding sites, site A, site B, and site C, are colored beige, cyan, and purple, respectively.

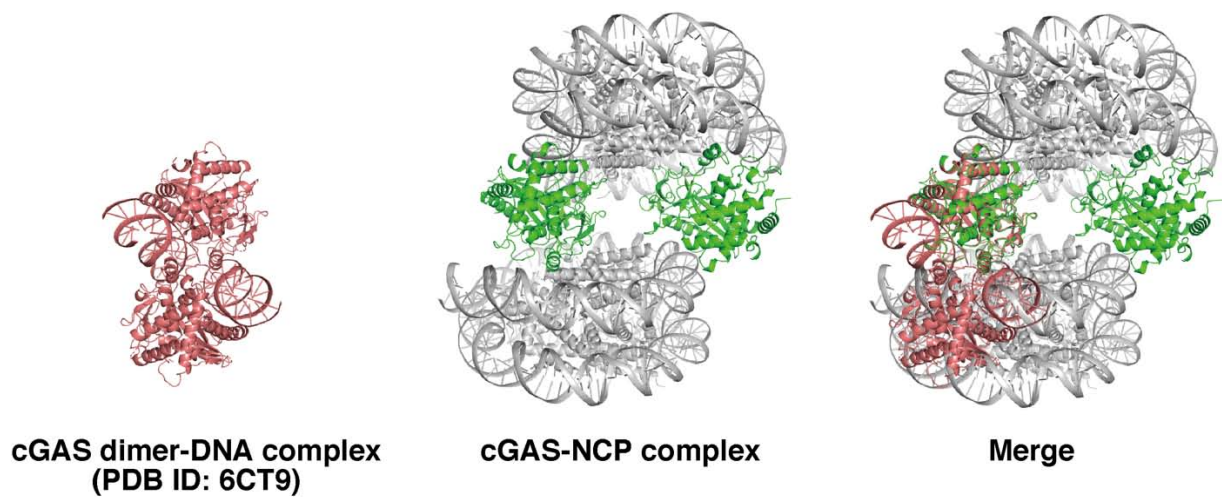


**Fig. S8. Dimerization of cGAS is inhibited by the NCP.** The cGAS dimer-DNA complex (left panel; colored salmon; PDB ID: 6CT9) and the cGAS-NCP complex (center panel; cGAS is colored green) were superimposed as shown in the right panel. Note the steric clash with the NCP that NCP-binding would cause.

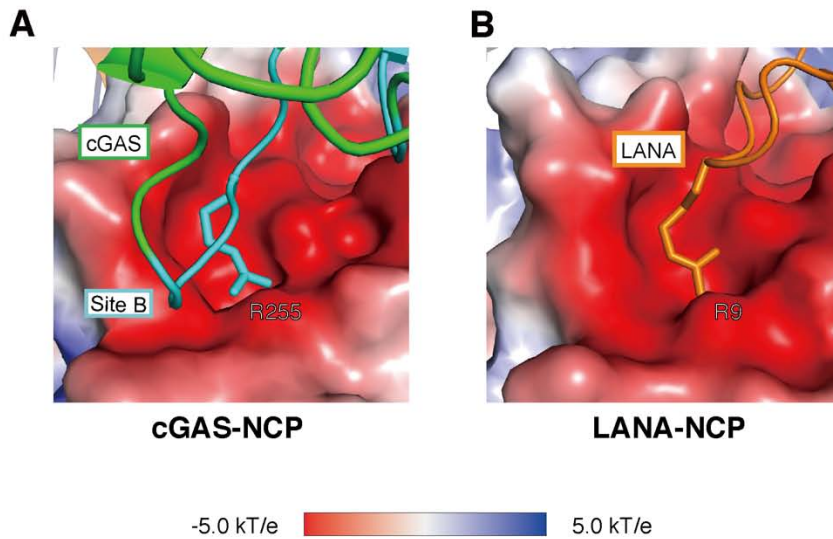


**Fig. S9. Arg255 of cGAS binds to the nucleosomal acidic patch with a similar conformation as the representative arginine anchor of the LANA peptide.** (A) Close-up view of Arg255 of cGAS complexed with the NCP. (B) Close-up view of Arg9 of Kaposi's sarcoma LANA peptide complexed with the NCP (PDB ID: 1ZLA). Surface electrostatic potential of NCPs (contoured from  $-5$  to  $+5$  kT/e) was calculated with the ABPS tool. Both arginine residues of cGAS and LANA bind the deeper pocket of the acidic patch.



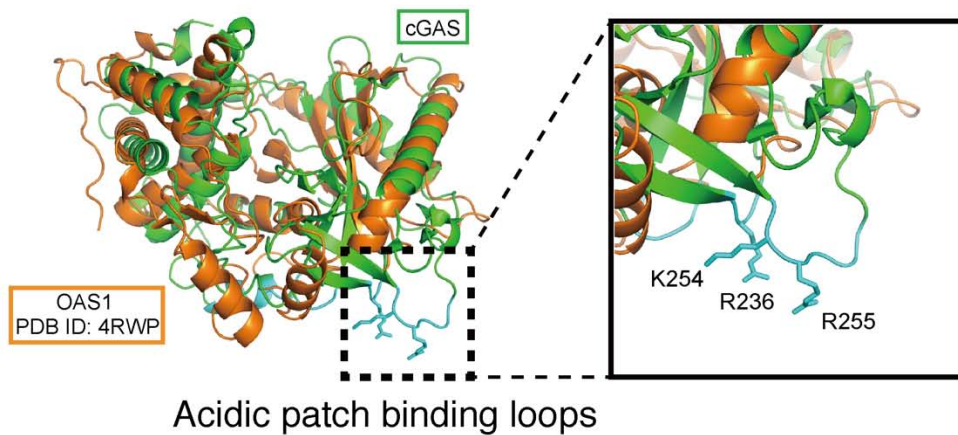


**Fig. S11. Comparison between OAS1 and cGAS structures.** OAS1 of the OAS1-dsRNA complex (colored orange; PDB ID: 4RWP) and human cGAS of the cGAS-NCP complex (colored green) are superimposed. Although the overall structure of OAS1 is similar to that of cGAS, the acidic patch binding loop region containing R236, K254, and R255 of cGAS is not conserved in OAS1.

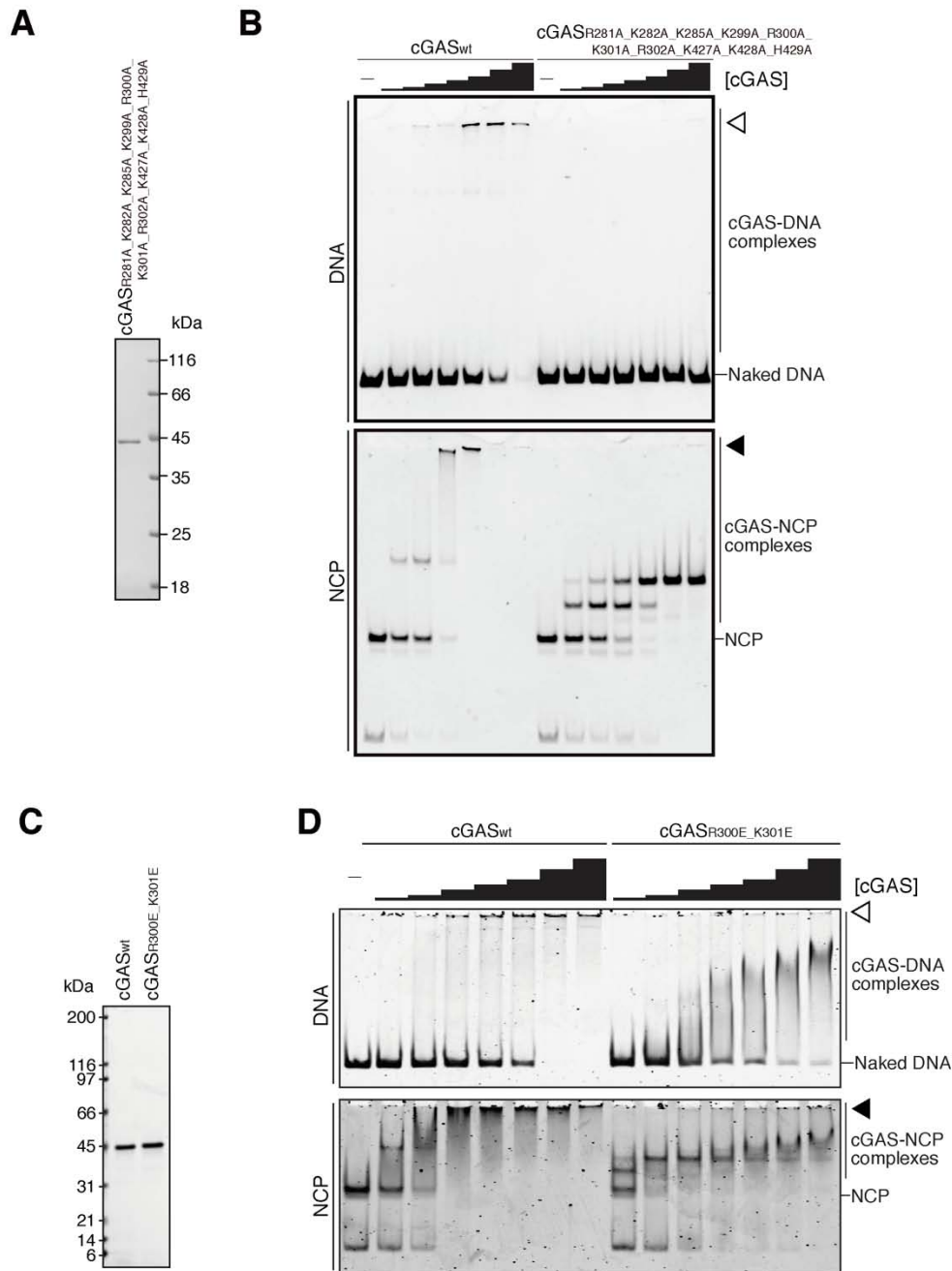


**Fig. S12. Binding assays with site C mutants.** (A) Purified cGAS<sub>R281A\_K282A\_K285A\_K299A\_R300A\_K301A\_R302A\_K427A\_K428A\_H429A</sub> was analyzed by SDS-PAGE and Coomassie Brilliant Blue staining. (B) Representative gel images of band shift assays of wt cGAS or cGAS<sub>R281A\_K282A\_K285A\_K299A\_R300A\_K301A\_R302A\_K427A\_K428A\_H429A</sub> with naked DNA or NCPs. The result was reproduced in two additional independent experiments. (C) Purified wt cGAS and cGAS<sub>R300E\_K301E</sub> were analyzed by SDS-PAGE and Coomassie Brilliant Blue staining. (D) Representative gel images of band shift assays of wt cGAS or cGAS<sub>R300E\_K301E</sub> with naked

DNA or NCPs. The result was reproduced in another independent experiment. White and black arrowheads indicate the cGAS-DNA multimer and the cGAS-NCP multimer, respectively.

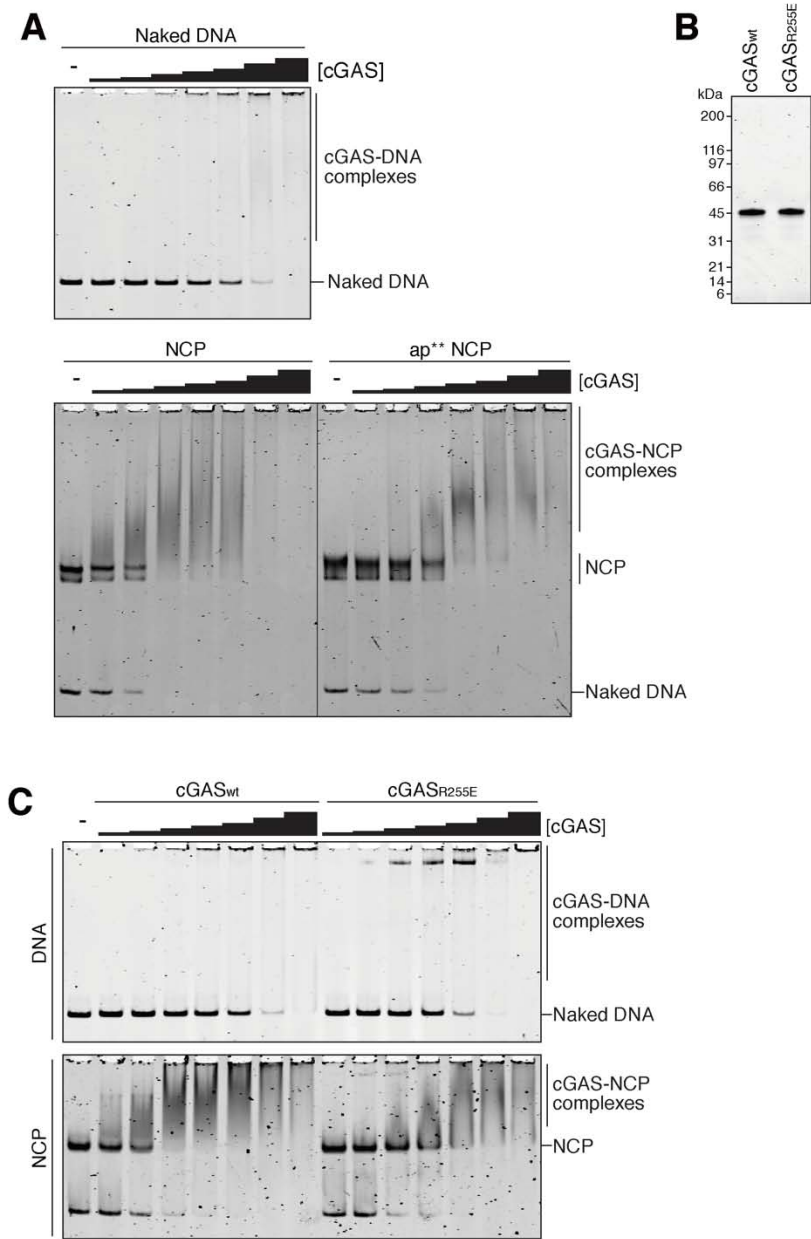


**Fig. S13. Representative data relating to the in vitro analysis of cGAS binding to NCPs and catalytic activity.** (A) Example gels of band shift assays of wt cGAS with naked DNA, wt NCPs, or acidic patch mutant (ap\*\*) NCPs. The vertical line indicates an empty lane that was removed. Four independent experiments were used for Fig. 4, A and B. (B) Coomassie stained gel of purified wt cGAS and cGAS<sub>R255E</sub>. (C) Example gels of band shift assays of naked DNA or NCPs with wt cGAS or cGAS<sub>R255E</sub>. Three independent experiments were used for Fig. 4C-E.

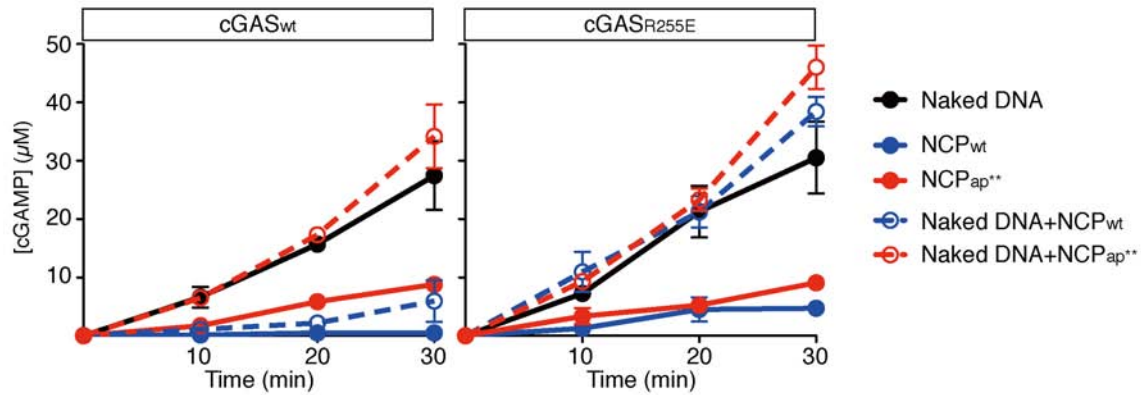


**Fig. S14. Quantification of cGAMP generation for determination of  $K_{cat}$  values in Fig. 4G.**

Quantifications of cGAMP generation with the indicated cGAS versions together with naked DNA, wildtype (wt) NCPs, or acidic patch mutated ( $ap^{**}$ ) NCPs in vitro. Averages and SEM (error bars) of three independent experiments are shown for each time point. Naked DNA and NCPs were 145 bp of DNA, and were used at 230 nM each.

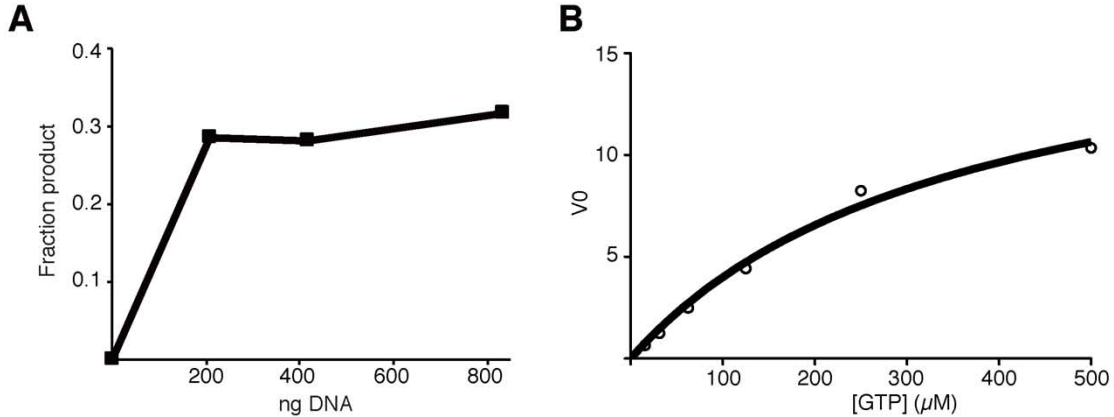


**Fig. S15. DNA and GTP titrations for the cGAMP generation assays.** As outlined in more detail in the Material and Methods, we carried out cGAMP generation assays under substrate saturation conditions, where the initial reaction velocity resembled  $V_{\text{max}}$ . This is verified for DNA amounts and GTP concentration by experiments shown in this figure. **(A)** Standard reactions with wild type cGAS and varying amounts of 601 DNA were performed. Note that all assays from Fig. 4G and fig. S17 were performed with 220 ng DNA. **(B)** Standard reactions with wild type cGAS and varying amounts of GTP DNA were performed. Note that all assays from Fig. 4G and fig. S17 were performed at 1 mM GTP concentration. Both experiments were carried out once.

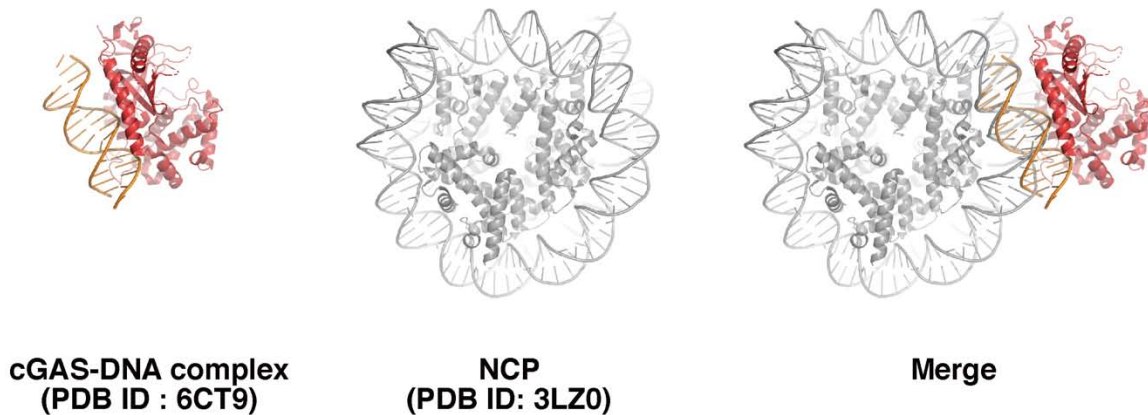


**Fig. S16. Representative images of DNA-bound cGAS superimposed onto the NCP.** The cGAS-DNA complex (left panel; PDB ID: 6CT9) and the NCP complex (middle panel; PDB ID: 3LZ0) were superimposed by DNA-based alignment as shown in the right panel. Note that DNA in the cGAS-DNA complex is in a straight conformation as opposed to the DNA conformation within the NCP.

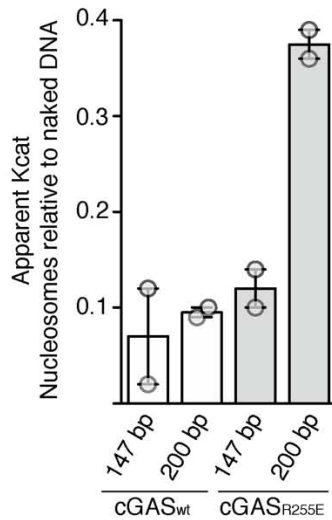


**Fig. S17. cGAMP generation by cGAS<sub>wt</sub> and cGAS<sub>R255E</sub> with nucleosomes with or without linker DNA.** cGAMP production assays were carried out with the indicated proteins and either naked DNA (147 bp and 200 bp) or nucleosomes assembled on the same DNA. Apparent Kcat values were determined and for each cGAS type and nucleosome type normalized to the equivalent reactions with naked DNA. Shown are means (bars) from two independent experiments (dots). Error bars: Range.

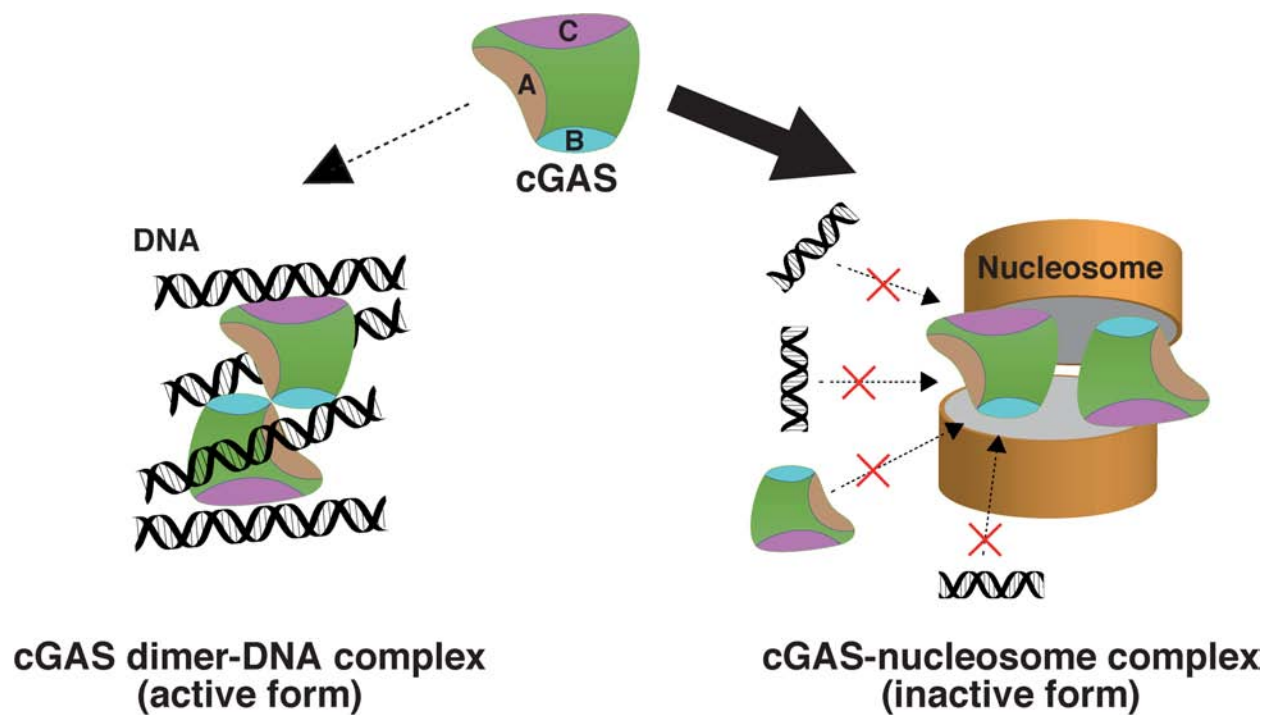


**Fig. S18. Model for cGAS inactivation by nucleosomes.** cGAS (green) preferentially binds nucleosomes (thick solid line arrow) rather than DNA (dotted arrow). cGAS binds exogenous DNA (colored black) as a dimer with three DNA-binding sites, site A (beige), site B (cyan), and site C (purple), activating cGAMP synthesis. In contrast, two cGAS monomers bind and bridge two nucleosomes (orange). In the cGAS-nucleosome complex, the three DNA-binding sites of cGAS become inaccessible to exogenous DNA, and dimerization of cGAS is suppressed. Consequently, cGAS molecules complexed with nucleosomes are inactivated.

Sample	Human cGAS-NCP cooemplex EMD-30267, PDB ID:7C0M
<b>Data collection</b>	
Electron microscope	Thermo Fisher Krios G3i
Camera	GATAN K3 Bioquantum (6k x 4k)
Pixel size (Å/pix)	1.05
Defocus range (µm)	-1.0 to -2.5
Exposure time (second)	5.6
Total dose (e/Å <sup>2</sup> )	64
Number of frames	40
Dose per frame (e/Å <sup>2</sup> /frame)	1.6
Number of collected micrographs	7066
Number of selected micrographs	6645
<b>Reconstruction</b>	
Number of initially autopicked particles	2,324,880
Number of particles used for classification	1,903,331
Number of particles in the final map	160,075
Symmetry	C1
Final resolution (Å)	3.9
FSC threshold	0.143
<b>Model composition</b>	
Protein	2234
Nucleotide	580
Ligands	2
<b>Validation</b>	
EMRinger score	1.06
MolProbity score	1.70
Clash score	5.92
CC(mask)	0.57
CC(box)	0.76
CC(volume)	0.59
CC(peaks)	0.55
RMSDs	
Bond length (Å)	0.011
Bond angle (°)	0.824
Ramachandran plot (%)	
Outliers	0.0
Allowed	5.51
Favored	94.49
Rotamer outliers (%)	0.73

**Table S1. Cryo-EM data collection, processing, and validation statistics.**

## Supplementary References

1. T. Kujirai, Y. Arimura, R. Fujita, N. Horikoshi, S. Machida, H. Kurumizaka, Methods for Preparing Nucleosomes Containing Histone Variants. *Methods Mol. Biol.* **1832**, 3-20 (2018).
2. D. Vasudevan, E. Y. Chua, C. A. Davey, Crystal structures of nucleosome core particles containing the '601' strong positioning sequence. *J. Mol. Biol.* **403**, 1-10 (2010).
3. Y. Arimura, H. Tachiwana, T. Oda, M. Sato, H. Kurumizaka, Structural analysis of the hexasome, lacking one histone H2A/H2B dimer from the conventional nucleosome. *Biochemistry* **51**, 3302-3309 (2012).
4. P. T. Lowary, J. Widom, New DNA sequence rules for high affinity binding to histone octamer and sequence-directed nucleosome positioning. *J. Mol. Biol.* **276**, 19-42 (1998).
5. D. N. Mastronarde, Automated electron microscope tomography using robust prediction of specimen movements. *J. Struct. Biol.* **152**, 36-51 (2005).
6. S. Q. Zheng, MotionCor2: anisotropic correction of beam-induced motion for improved cryo-electron microscopy. *Nat. Methods* **14**, 331-332 (2017).
7. K. Zhang, Gctf: Real-time CTF determination and correction. *J. Struct. Biol.* **193**, 1-12 (2016).
8. J. Zivanov, T. Nakane, B. O. Forsberg, D. Kimanius, W. J. Hagen, E. Lindahl, S. H. Scheres, New tools for automated high-resolution cryo-EM structure determination in RELION-3. *eLife*. **7**, e42166 (2018).
9. Y.Z. Tan, P.R. Baldwin, J.H. Davis, J.R. Williamson, C.S. Potter, B. Carragher, D. Lyumkis, Addressing preferred specimen orientation in single-particle cryo-EM through tilting. *Nat. Methods*, **14**, 793–796 (2017).
10. E. Ramírez-Aportela, J. L. Vilas, A. Glukhova, R. Melero, P. Conesa, M. Martínez, D. Maluenda, J. Mota, A. Jiménez, R. J. Vargas, Marabini, P. M. Sexton, J. M. Carazo, C. O. S. Sorzano, Automatic local resolution-based sharpening of cryo-EM maps. *Bioinformatics* **36**, 765-772 (2020).
11. J. L. Vilas, J. Gómez-Blanco, P. Conesa, R. Melero, J. Miguel de la Rosa-Trevín, J. Otón, J. Cuenca, R. Marabini, J. M. Carazo, J. Vargas, C. O. S. Sorzano, MonoRes: Automatic and accurate estimation of local resolution for electron microscopy maps. *Structure* **26**, 337-344 (2018).
12. J. M. de la Rosa-Trevín, A. Quintana, L. Del Cano, A. Zaldívar, I. Foche, J. Gutiérrez, J. Gómez-Blanco, J. Burguet-Castell, J. Cuenca-Alba, V. Abrishami, J. Vargas, J. Otón, G. Sharov, J. L. Vilas, J. Navas, P. Conesa, M. Kazemi, R. Marabini, C. O. Sorzano, J. M. Carazo, Scipion: A software framework toward integration, reproducibility and validation in 3D electron microscopy. *J. Struct. Biol.* **195**, 93-99 (2016).
13. D. N. Kim, N. W. Moriarty, S. Kirmizialtin, P. V. Afonine, B. Poon, O. V. Sobolev, P. D. Adams, K. Sanbonmatsu, *Cryo\_fit*: Democratization of flexible fitting for cryo-EM. *J. Struct. Biol.* **208**, 1-6 (2019).
14. P. Emsley, B. Lohkamp, W. G. Scott, K. Cowtan, Features and development of Coot. *Acta Crystallogr. D Biol. Crystallogr.* **66**, 486-501 (2010).
15. D. Lieschner, P. V. Afonine, M. L. Baker, G. Bunkóczi, V. B. Chen, T. I. Croll, B. Hintze, L.

- W. Hung, S. Jain, A. J. McCoy, N. W. Moriarty, R. D. Oeffner, B. K. Poon, M. G. Prisant, R. J. Read, J. S. Richardson, D. C. Richardson, M. D. Sammito, O. V. Sobolev, D. H. Stockwell, T. C. Terwilliger, A. G. Urzhumtsev, L. L. Videau, C. J. Williams, P. D. Adams, Macromolecular structure determination using X-rays, neutrons and electrons: recent developments in Phenix. *Acta Crystallogr. D Struct. Biol.* **75**, 861-877 (2019).
16. C. J. Williams, J. J. Headd, N. W. Moriarty, M. G. Prisant, L. L. Videau, L. N. Deis, V. Verma, D. A. Keedy, B. J. Hintze, V. B. Chen, S. Jain, S. M. Lewis, W. B. 3rd Arendall, J. Snoeyink, P. D. Adams, S. C. Lovell, J. S. Richardson, D. C. Richardson, MolProbity: More and better reference data for improved all-atom structure validation. *Protein Sci.* **27**, 293-315 (2018).
  17. B.A. Barad, N. Echols, R.Y. Wang, Y. Cheng, F., DiMaio, P.D. Adams, J. S. Fraser, EMRinger: side chain-directed model and map validation for 3D cryo-electron microscopy. *Nat. Methods* **12**, 943-946 (2015).
  18. E. F. Pettersen, T. D. Goddard, C. C. Huang, G. S. Couch, D.M. Greenblatt, E. C. Meng, T. E. Ferrin, UCSF Chimera--a visualization system for exploratory research and analysis. *J. Comput. Chem.* **25**, 1605-1612 (2004).
  19. A.W. Murray, Cell cycle extracts. *Methods Cell Biol.* **36**, 581-605 (1991).